The Canadian Mineralogist
Vol. 51, pp. 313-332 (2013)
DOI: 10.3749/canmin.51.2.313

NACARENIOBSITE-(Ce) AND BRITHOLITE-(Ce) IN PERALKALINE GRANITES FROM THE MORRO REDONDO COMPLEX, GRACIOSA PROVINCE, SOUTHERN BRAZIL: OCCURRENCE AND COMPOSITIONAL DATA

Frederico C. J. VILALVA[§] and Silvio R.F. VLACH

Instituto de Geociências, Universidade de São Paulo, São Paulo SP 05508-080, Brazil

Antonio SIMONETTI

Department of Civil Engineering and Geological Sciences, University of Notre Dame, Notre Dame IN 46556, USA

Abstract

Nacareniobsite-(Ce), $Na_3Ca_3(REE)Nb(Si_2O_7)_2OF_3$, and britholite-(Ce), $(Na,Ca,REE)_{10}(Si,P)_6O_{24}(OH,F)_2$, formed during the late stages of crystallization of the most evolved peralkaline granites from the Morro Redondo Complex, Graciosa Province (Southern Brazil). Nacareniobsite-(Ce) compositions are very close to ideal, with Na_2O and Nb_2O_5 contents up to 11.1 and 15.5 wt.%, respectively, corresponding to an average formula of $Na_{3.0}(Ca_{2.75}Sr_{0.01})_{\Sigma 2.76}(REE,Y)_{1.16}(Nb_{0.95}Ta_{0.02}Ti_{0.04})_{\Sigma 1.01}Si_{3.99}O_{14}(O_{1.11}F_{2.89})_{\Sigma 4}$. Compared to the host rock composition, trace-element patterns for nacareniobsite-(Ce) indicate enrichment in REEs and Sr, and depletion in alkali metals and Zr. The available chemical data are in excellent agreement with a complete solid solution series between rinkite and nacareniobsite-(Ce), controlled by $[M^{+4}M^{2+}]_{-1}[M^{5+}Na^{+}]$ and, in part, $[M^{2+}]_{-2}[REE^{3+}Na^{+}]$ and $[M^{+4}M^{2+}]_{-1}[REE^{3+}]_2$ exchange vectors. Britholite-(Ce) compositions are amongst the most (REE,Y)-enriched reported to date, with REE + Y contents up to 73.6 wt.% oxide. REE and trace element distributions relative to the host rock exhibit some similarities with those observed for nacareniobsite-(Ce); however, Ba, Th, U, and Pb contents are relatively higher. The observed compositions agree very well with $[PM^{2+}F]_{-1}[Si(REE,Y)(OH)]$, $[M^{2+}]_{-2}[Na(REE,Y)]$, and $[M^{2+}(Th,U)]_{-1}[(REE,Y)]_2$ exchange vectors. Crystallization of both minerals was favored by the F-, Na-, and HFSE-enriched nature and moderate-to-strong peralkaline signature of the melt, at temperatures below 600 °C in a relatively reduced environment.

Keywords: nacareniobsite-(Ce), britholite-(Ce), EPMA and LA-ICP-MS analysis, peralkaline granites, Morro Redondo Complex, Graciosa Province, Brazil

Introduction

Nacareniobsite-(Ce), a sorosilicate with ideal formula $Na_3Ca_3(REE)Nb(Si_2O_7)_2OF_3$, was first described by Petersen *et al.* (1989) in lujavrites from the Ilímaussaq alkaline complex, South Greenland (see also Pekov & Ekimenkova 2001). It was included in the rinkite series, constituted by the Na-Ca-REE-Ti-Nb silicates rinkite, rincolite, johnstrupite, and lovchorrite, as defined by Slepnev (1957), who also described mosandrite as an alteration product of these minerals. Fleischer (1958) argued that the rinkite series minerals should be discredited in favor of mosandrite, given its precedence. Sokolova & Cámara (2008) determined the structure of mosandrite from the type locality and demonstrated that its chemical composition and structural topology are identical to that of rinkite (Galli & Alberti 1971). Thus, Cámara *et al.* (2011) concluded that mosandrite requires redefinition. Accordingly, the mineral name rinkite will be adopted in this work.

Nacareniobsite-(Ce) is a very rare mineral, described in some detail in only three other occurrences of alkaline undersaturated rocks in the world: Mecsek Mountains, Hungary (Nagy 2003), Los Isle, Guinea (Parodi & Chevrier 2004), and Kilombe volcano, Kenya (Ridolfi *et al.* 2006). More recently, it was reported in oversaturated rocks within peralkaline granites from the complexes of Morro Redondo, Brazil (Vlach & Vilalva 2007) and Ambohimirahavavy, Madagascar (Estrade *et al.* 2011). The $P2_1/a$ space group symmetry was assigned by Petersen *et al.* (1989) to the holotype species; however, based on an investigation of a sample from the same locality, Sokolova & Hawthorne (2008) concluded that the nacareniobsite-(Ce) structure better conforms to the

§ *E-mail address*: fredcjv@me.com (corresponding author)

$P2_1/c$ space group. These authors also classified it as a Group-I mineral with the so-called TS (titanium silicate) block (see also Sokolova 2006), with a corresponding structural formula of $A^P{}_2M^H{}_2M^O{}_4(Si_2O_7)_2X^O{}_4$. Sokolova & Hawthorne (2008) state also that this is the sole mineral with a pentavalent cation that is dominant at one site ($M^O{}_{(1)}$) amongst the M^O positions within the O sheet constituting these blocks.

Britholite, first described by Winther (1901), is a REE-rich mineral with general formula (Na,Ca, REE)$_{10}$(Si,P)$_6$O$_{24}$(OH,F)$_2$ and Si > P (Oberti *et al.* 2001). It is a relatively common accessory mineral in alkaline, specially undersaturated rocks, and in some granites and pegmatites, as well as in several related metasomatites (*e.g.*, Fleischer & Altschuler 1986, Arden & Halden 1999, Oberti *et al.* 2001, Pekov *et al.* 2007, Melluso *et al.* 2012); in the latter, at times, it can occur in ore quantities, as in skarns associated with syenite gneiss at Kipawa, Quebec, Canada (Lentz & Mariano 2010). Britholite was considered to be isostructural with apatite and has been classified both as an apatite-group mineral or belonging to an independent mineral group (Gaines *et al.* 1997, Strunz & Nickel 2001, Pan & Fleet 2002). In the latter case, it constitutes two series (Pekov *et al.* 2007): the britholite series *stricto sensu*, with $\sum$(REE) > Ca *apfu*, and the calciobritholite series, in which $\sum$(REE) < Ca *apfu*. Both series include relatively F-rich species: fluorbritholite and fluorcalciobritholite (Gu *et al.* 1994, Pekov *et al.* 2007). The nomenclature of the apatite minerals was recently rationalized by the IMA, which considers britholite minerals as a proper group within the apatite supergroup (Pasero *et al.* 2010). According to Oberti *et al.* (2001), the structure of britholite-(Ce) is better defined by the 6_3 rather than the $6_3/m$ space group, which is typical of apatite and fluorcalciobritholite (Pekov *et al.* 2007). Based on Oberti *et al.* (2001), the britholite-(Ce) structure is characterized by one tetrahedral, one $(REE)_2$ unique site, and two independent $(REE)_1$ and $(REE)_{1a}$ degenerated sites.

Among the peralkaline granites associated with the A-type granites and syenites from the Neoproterozoic Graciosa Province, Southern Brazil (Gualda & Vlach 2007), some of the most evolved types that crop out in the Morro Redondo Complex are unique and particularly interesting from a mineralogical perspective. They contain several rare Ti-, HFSE-, and REE-bearing minerals, which define agpaitic parageneses formed in most of the cases in late- to post-magmatic crystallization stages. With the exception of some as-yet poorly described [*e.g.,* gerenite-(Y) and kuannersuite-(Ce) ?] or even unidentified minerals, those that have been reported include: chevkinite, allanite, aenigmatite, astrophyllite, narsarsukite, nacareniobsite-(Ce), britholite-(Ce), REE-rich turkestanite, neptunite, elpidite and other (Na,K) zirconosilicates, and bastnäsite (Vilalva 2007, Vlach & Gualda 2007, Vlach & Vilalva 2007, Vilalva & Vlach 2010).

Building on previous work (*e.g.*, Vlach & Gualda 2007, Vilalva & Vlach 2010, Vlach 2012) in relation to the mineralogy of peralkaline granites from the Graciosa Province, this study reports detailed and combined new textural and compositional (EPMA, LA-ICP-MS) data for nacareniobsite-(Ce) and britholite-(Ce) from peralkaline granites of the Morro Redondo Complex, and these are compared to literature data. This contributes to our knowledge of their major and trace element content variations, and to the mineralogical description of the Province as a whole.

Geological Background

The Morro Redondo Complex occupies ~250 km^2 and is one of the largest occurrences of A-type granites and syenites in the Graciosa Province (Vilalva 2007, Vlach & Gualda 2007). This Neoproterozoic magmatic province was emplaced under an extensional tectonic environment that characterized the evolution of Gondwana in this region at *ca.* 580 Ma (Vlach *et al.* 2011). Besides typical bimodal basic and acid volcanism, the Morro Redondo Complex consists of two main intrusive units: the Papanduva and Quiriri Plutons (Fig. 1, see also Vilalva & Vlach 2010, 2013). The former is smaller and consists of a variety of peralkaline alkali-feldspar granites (Alkaline Association), whereas the latter contains aluminous, subalkalic, mainly biotite syenogranites (Aluminous Association; Gualda & Vlach 2007). General background geology and petrography, as well as additional details, in particular relating to the geochemical aspects of the complex, may be found in Vilalva & Vlach (2013).

The locations of nacareniobsite-(Ce) and britholite-(Ce)-bearing samples, including those selected for this work (MR-02, MR-02A, MR-03, and MR-140), are given in Figure 1. They are representative of the oriented, white to gray, petrographic facies (unit A of Vilalva & Vlach 2010) which crops out at the NE-N-NW borders of the Papanduva Pluton (Fig. 1), and is characterized by well-developed deformational structures, giving the rocks a 'protomylonitic' aspect (Fig. 2). They consist of deformed and oriented, ellipsoidal to irregular alkali feldspar, arfvedsonite and rare quartz megacrystals (up to 4.0 mm) in a fine-grained saccharoidal matrix with quartz, microcline, albite, fluorite, aegirine, some arfvedsonite, and combinations of several rare accessory minerals, as listed above (Fig. 2B). Several of the observed textures suggest that, despite the 'protomylonitic' rock appearance, deformation occurred at least in part under sub-magmatic conditions, involving flow of melting and crystal mushes, with crystal plastic deformation (Blenkinsop 2000, Passchier & Trouw 2005), rather than in solid-state conditions; these include: bent alkali feldspar crystals with microfractures filled by late melts (now fine-grained aggregates of quartz and feldspar), undulose

extinction in quartz from the matrix, along with typical core-to-rim compositional zoning in arfvedsonite and aegirine, and millimetric- to centimetric-sized vugs and miarolitic cavities (sometimes partially filled with post-magmatic minerals).

These granites followed an agpaitic crystallization sequence, where mafic and accessory minerals began to crystallize after the felsic minerals. Several of the mafic and most of the rare accessory minerals were, in fact, formed during late- to post-magmatic crystallization stages (*e.g.*, Vilalva & Vlach 2010, 2013). The modal abundances of mafic minerals in the studied samples are up to 10% and, among them, up to 4% are of rare accessories.

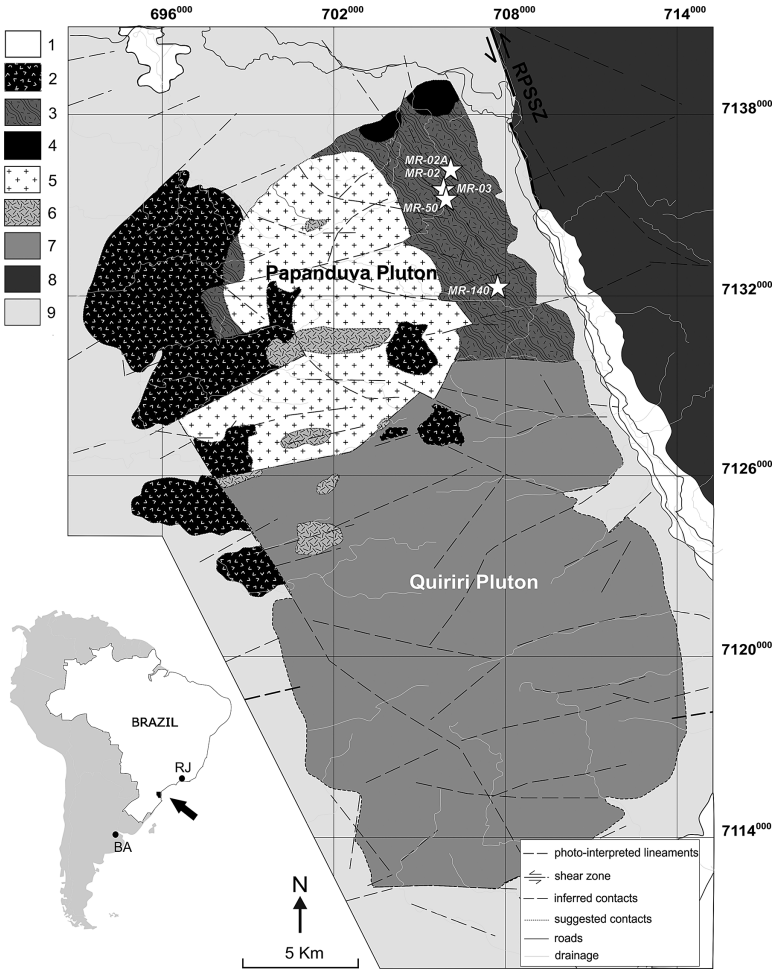

FIG. 1. Simplified geologic map of the Morro Redondo Complex and surrounding areas in Southern Brazil showing the location of nacareniobsite-(Ce)- and britholite-(Ce)-bearing samples (white stars: samples MR-02, MR-02A and MR-140 and MR-03 and MR-50, respectively) from peralkaline granites of the Papanduva Pluton. (1) alluvial-colluvial deposits, (2) contemporaneous acid and basic volcanic rocks; (3 to 6) peralkaline alkali-feldspar granites from the Papanduva Pluton: (3) deformed 'protomylonitic' facies, (4) deformed 'cataclastic' facies, (5) massive facies, (6) microgranitic facies; (7) peraluminous biotite syenogranites from the Quiriri Pluton; (8) metasedimentary rocks of the Neoproterozoic Paranaguá Terrain; (9) gneiss, granulites and migmatites of the Archean Luiz Alves Terrain. RPSSZ: Rio Palmital-Serrinha Shear Zone. Inset shows the positioning of the Complex into the South American Continent (RJ = Rio de Janeiro, Brazil; BA = Buenos Aires, Argentina).

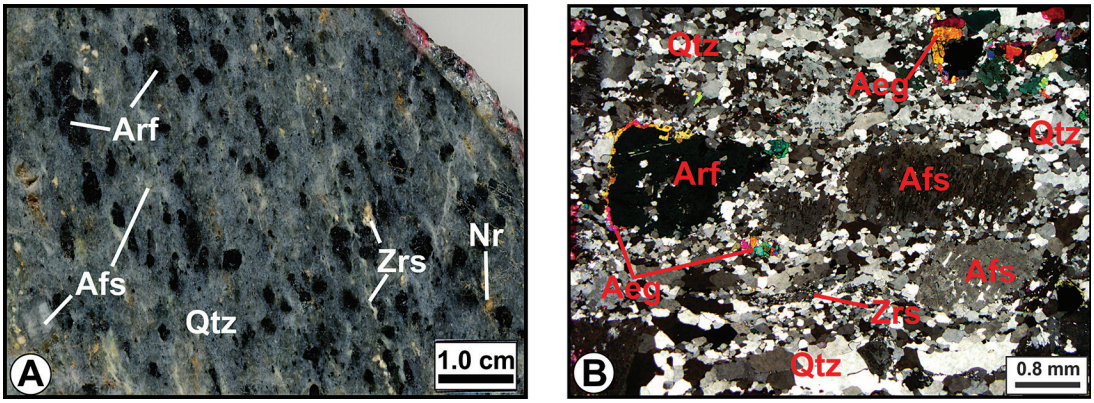

FIG. 2. Meso- and microscopic textural features of the sub-magmatic deformed peralkaline alkali-feldspar granite of the Papanduva Pluton, Morro Redondo Complex (sample MR-03). (A) Macroscopic 'protomylonitic' aspect defined by elongated and rounded arfvedsonite and alkali feldspar megacrystals in a fine-grained quartzofeldspathic matrix. Note elongated crystals of narsarsukite and unidentified (Na,K)-zirconosilicates parallel to foliation. (B) Microtextural 'protomylonitic' aspect under crossed polarizers showing alkali feldspar and arfvedsonite deformed megacrystals, the latter mantled by aegirine, in a fine-grained, quartz-rich matrix with microcline and albite (not shown), aegirine, arfvedsonite, and rare accessory minerals such as unidentified (Na,K)-zirconosilicates. Qtz: quartz; Afs: alkali feldspar; Arf: arfvedsonite; Nr: narsarsukite; Zrs: unidentified (Na,K)-zirconosilicates; Aeg: aegirine.

The geochemical signatures of these alkali feldspar granites are typical of A-type evolved peralkaline granites documented elsewhere, with high fe# numbers [$FeO^T/(FeO^T + MgO)$, wt.% oxides] and agpaitic indexes [$(Na_2O + K_2O)/Al_2O_3$], up to 0.99 and 1.30 molar, respectively, as well as relatively high abundances of alkali metals and high field strength elements (HFSEs; see Vilalva & Vlach 2013). As expected, abundances for most HFSEs show well-defined positive correlations with the Agpaitic Index. All samples present low magnetic susceptibilities ($< 10^{-3}$ SI) and many of them are high heat producing (HHP) granites, with heat production per unit volume up to 5.7 μWm^{-3}. Representative whole rock data for nacareniobsite-(Ce)- and britholite-(Ce)-bearing samples studied in this work are given in Table 1.

ANALYTICAL METHODS AND DATA TREATMENT

Compositional data for nacareniobsite-(Ce) and britholite-(Ce) were obtained from 30–80 μm thick polished thin sections by Electron Probe Microanalysis (EPMA) at the GeoAnalítica-USP Facility, Instituto de Geociências, Universidade de São Paulo, Brazil. Laser Ablation Inductively Coupled Plasma Mass Spectrometry (LA-ICP-MS) analyses were conducted at the MITERAC Facility, University of Notre Dame, USA.

Electron probe microanalyses

Wavelength Dispersive Spectrometry (WDS) analyses were obtained using a JEOL-JXA8600S equipped with 5 wavelength and 1 energy dispersive spectrometers and automated by the Thermo-Noran Voyager 4.3.1 system. Operating conditions were 15 kV, 20 nA, and 5–10 μm for the column accelerating voltage, beam current, and beam diameter, respectively. Backscattered electron (BSE) compositional imaging was systematically used to monitor crystal compositional variations not detected in thin sections and to select spots for analysis. The analyzed elements and analytical conditions were chosen after precise qualitative WDS scans over typical nacareniobsite-(Ce) and britholite-(Ce) grains. The quantified spectral lines, analyzer crystals and standards employed for nacareniobsite-(Ce) were: Si*K*α (PET, osumilite), Zr*L*α (PET, ZrO_2),Th*M*α (PET, ThO_2), Ti*K*α (LIF, titanite), Al*K*α (TAP, YAlG), La*L*α, Ce*L*α, Pr*L*β, Nd*L*β, Sm*L*β, Gd*L*β, and Dy*L*β [LIF, (REE)PO_4, Jarosewich & Boatner 1991], Y*L*α (PET, YAlG), Fe*K*α and Mn*K*α (LIF, Mn-olivine), Ca*K*α (PET, titanite), Sr*L*α (PET, $SrTiO_3$), Ba*L*α (PET, $BaAl_2Si_2O_8$), Na*K*α (TAP, jadeite), Nb*L*α (PET, Nb metal), Ta*L*α (LIF, Ta metal), and F*K*α (TAP, F-apatite). Similar settings were used for britholite; though Zr, Ti, Mg, Sr, Nb, and Ta were not analyzed, while U*M*β (PET, UO_2), Yb*L*α (LIF, $YbPO_4$), and P*K*α (PET, $CePO_4$) were added to the analytical routine, and $BaAl_2Si_2O_8$ was used as the main Si standard. Total count times, equally divided between peak and background measurements, were variable from 5 for the lightest to 80 s for the heaviest elements present in small contents. The PROZA program (*e.g.*, Bastin & Heijligers 1990) was used for matrix correction and data reduction. Spectral interferences of Ce over F and Th over U were corrected

as described by Vlach (2010). The estimated relative analytical precision, as verified with standards, is better than 2% and up to 10% for the major and minor elements, respectively, and ≤ 0.01 wt.% oxide for the trace elements.

Structural formulae were computed on the basis of 18 (O + F) for nacareniobsite-(Ce) and 26 (O,F) for britholite-(Ce), following Cámara *et al*. (2011) and Oberti *et al*. (2001), respectively.

Laser Ablation-Inductively Coupled Plasma Mass Spectrometry

Trace element abundances were determined using a ThermoFinnigan high-resolution Element2 ICP-MS instrument coupled to a nanosecond ESI-New Wave Research UP213 laser ablation system. Laser spots were located over the most homogeneous areas within crystals, as delineated in BSE images. Nonetheless, the spatial resolution of the analysis is significantly lower when compared with that employed for EPMA, and consequently the total volumes sampled are much higher. Ablation experiments were carried out using an energy fluence of ~10 J/cm^2, repetition frequency of 4 Hz, and spot size of 30 μm. Helium flow rate within the laser ablation cell was ~0.70 l/minute. Total acquisition time was 120 s, divided equally between background and laser ablation ion signal measurements (8 ms dwell time for each isotope), followed by ~30 s of washout time. The ion signals for the following isotopes were measured for both minerals: ^{7}Li, ^{43}Ca, ^{45}Sc, ^{49}Ti, ^{51}V, ^{52}Cr, ^{55}Mn, ^{59}Co, ^{60}Ni, ^{65}Cu, ^{71}Ga, ^{85}Rb, ^{88}Sr, ^{90}Zr, ^{118}Sn, ^{133}Cs, ^{137}Ba, ^{147}Sm, ^{151}Eu, ^{155}Gd, ^{159}Tb, ^{163}Dy, ^{165}Ho, ^{166}Er, ^{169}Tm, ^{173}Yb, ^{175}Lu, ^{179}Hf, ^{181}Ta, ^{208}Pb, ^{232}Th, and ^{238}U. Moreover, ^{66}Zn, ^{139}La, ^{140}Ce, ^{141}Pr, and ^{143}Nd; ^{9}Be, ^{25}Mg and ^{93}Nb were also measured for nacareniobsite-(Ce) and britholite-(Ce), respectively. The NIST SRM 612 glass wafer was used as the external standard, while CaO wt.% contents obtained by EPMA were employed as internal standards. Data reduction and elemental abundance determinations were calculated using the Glitter software (van Achterbergh *et al*. 2001). Overall, the internal relative precision for all the elements investigated here ranges between 5 and 10% (2σ level).

Microscopy and Textural Environment

Nacareniobsite-(Ce) occurs in the matrix of some oriented peralkaline granite samples exhibiting submagmatic, close-to-solidus deformation textures (Fig. 2). It is associated with quartz, microcline, and albite in a fine-grained saccharoidal matrix with some arfvedsonite and aegirine as thin prismatic crystals. Crystals are typically small (< 1.0 mm). Two main textural generations are recognized: the first is idiomorphic to subidiomorphic, platy to prismatic, forming isolated and fractured crystals (Figs. 3A to 3D); the second consists of fibrous aggregates made up of thin crystal laths (Figs. 3A, 3E, 3F) that sometimes can overgrow the neighboring larger crystals (Figs. 3E, 3F). Under transmitted light, first generation crystals are transparent, homogeneous, and display both high relief (in relation to the felsic minerals) and a second-order yellow interference color (Figs. 3A, 3B). A subtle pleochroism, from colorless to very light pink, may be seen in some sections, and this feature serves to contrast nacareniobsite-(Ce) from colorless to very light green aegirine thin crystals. Back-scattered electron compositional imaging reveals that, in general, nacareniobsite-(Ce) is characterized by remarkable patchy zoning, as well as minute internal irregular areas with higher back-scattered coefficients consisting of unidentified Nb-rich minerals (Fig. 3C).

Britholite-(Ce) is rarer than nacareniobsite-(Ce) and occurs mostly as idiomorphic, isolated, and usually broken crystals (between 0.1 and 0.3 mm) exhibiting hexagonal basal sections that resemble common apatite (Figs. 4A, 4B). It is associated with quartz, alkali feldspars, and occasionally with narsarsukite (Fig. 4C). Crystals are optically homogeneous, uniaxial (–), colorless to creamy-colored, and exhibit high relief and a typical anomalous low-order, bluish to grayish interference color (Fig. 4). Back-scattered electron images display discrete compositional zoning (Fig. 4D). Some crystals show a spongy texture at their external rims as a result of alteration and partial substitution of britholite-(Ce) by bastnäsite through dissolution-precipitation-like processes probably occurring in a late hydrothermal event (Fig. 4D).

Textures indicate that (at the very least) the broken britholite-(Ce) crystals formed before close-to-solidus deformation and recrystallization of the previously formed quartz and alkali feldspar; in contrast, most nacareniobsite-(Ce) crystals seem to be post-deformation phases. Of note, despite the fact that both nacareniobsite-(Ce) and britholite-(Ce) occur in the same petrographic unit, from samples located proximal to one another in the field, britholite-(Ce) was not observed in any of the nacareniobsite-(Ce)-bearing samples. Table 2 lists coexisting accessory minerals in the studied samples, as well as their average REE contents. These include narsarsukite, elpidite, and unidentified (Na, K)-zirconosilicates, which crystallized relatively early and thus are deformed.

Compositional Variations

Three nacareniobsite-(Ce) and four britholite-(Ce) crystals were analyzed for this work, with a total of 16 and 18 WDS spots, respectively, and 6 LA-ICP-MS spots for each mineral. Representative compositions and structural formulae are listed in Tables 3 and 5; trace element abundances are reported in Tables 4 and

TABLE 1. WHOLE-ROCK CHEMICAL COMPOSITIONS FOR NACARENIOBSITE-(Ce)- AND BRITHOLITE-(Ce)-BEARING SAMPLES MR-02 AND MR-03 FROM THE PAPANDUVA PLUTON, MORRO REDONDO COMPLEX

Oxides (wt.%)	MR-02	MR-03	Elements (ppm)	MR-02	MR-03
SiO_2	75.38	74.55	Li	73.2	178.6
TiO_2	0.161	0.163	Be	11.0	9.40
Al_2O_3	10.58	9.89	Ga*	33	36
$Fe_2O_3^T$	3.85	5.62	Zn*	199	347
MnO	0.059	0.084	Rb	195	302
MgO	0.03	0.03	Sr	4.92	4.77
CaO	0.23	0.15	Y	165	323
Na_2O	4.68	5.24	Zr*	1798	2428
K_2O	4.33	3.77	Nb	52.4	88.1
P_2O_5	0.008	0.007	Cs	1.34	1.25
L.O.I.	0.32	0.34	Ba	28.5	16.2
			La	94.1	119
Total	**99.84**	**99.63**	Ce	177	233
			Pr	21.8	30.1
			Nd	82.8	119
fe#	0.991	0.994	Sm	20.1	31.8
ASI	0.826	0.762	Eu	0.80	1.34
AI	1.17	1.28	Gd	21.7	39.1
			Tb	3.78	6.78
			Dy	24.3	43.0
fe# = $FeO^T/(FeO^T + MgO)$			Ho	5.27	9.19
(% wt. oxides)			Er	15.7	26.1
			Tm	2.31	3.73
ASI = $Al_2O_3/(CaO + Na_2O + K_2O)$			Yb	15.4	24.1
(moles)			Lu	2.29	3.46
			Hf	46.4	61.2
AI = $(Na_2O + K_2O)/Al_2O_3$			Pb	39.5	88.3
(moles)			Th	32.4	47.9
			U	6.20	7.81

Major and minor elements by X-ray fluorescence, trace elements by X-ray fluorescence (*) and ICP-MS (see also Vilalva & Vlach 2013).

6. Complementary EPMA and LA-ICP-MS analyses can be obtained from the principal author. The main geochemical signatures and compositional variations of these two minerals are discussed relative to the best available data from other occurrences (*cf.* Tables 3, 5) as well as to the whole-rock geochemical data (Table 1).

Nacareniobsite-(Ce)

Chemical data for nacareniobsite-Ce, rinkite, and 'mosandrite' are listed in Table 3. Nacareniobsite-(Ce) from the Morro Redondo Complex is relatively homogeneous and, compared to literature data, most closely approaches the ideal endmember composition with $10.7 \leq Na_2O \leq 11.1$ wt.% (2.67–3.06 *apfu*) and $14.8 \leq Nb_2O_5+Ta_2O_5 \leq 15.8$ wt.% (0.93–0.99 *apfu*). The calculated mean formula, based on 16 analyses, is $Na_{3.0}(Ca_{2.75}Sr_{0.01})_{\Sigma 2.76}(REE,Y)_{1.16}(Nb_{0.95}Ta_{0.02}Ti_{0.04})_{\Sigma 1.01}Si_{3.99}O_{14}(O_{1.11}F_{2.89})_{\Sigma 4}$. In general, lathy crystals that form fibrous aggregates contain slightly higher TiO_2 and REEs and lower Nb_2O_5 and Ta_2O_5 than the earlier-formed ones (*cf.* Table 3, spots f_2i, f_3i).

Based on ideal formulae and available data, Petersen *et al.* (1989) suggested an extensive solid solution series between the endmembers rinkite, with the ideal formula $Na_2Ca_4(REE)Ti(Si_2O_7)_2OF_3$, and nacareniobsite-(Ce), related by the $[Ti^{+4}Ca^{2+}]_{-1}[Nb^{5+}Na^{+}]$ coupled exchange substitution. The authors also indicate that the observed compositional variations among the rinkite-related minerals, such as rinkolite and götzenite, follow the $[Ca^{2+}]_{-2}[REE^{3+}Na^{+}]$ substitution. Recently, Cámara *et al.* (2011) showed that the available rinkite and nacareniobsite-(Ce) compositions lie on a plane within (Nb,Ta-REE,Y,Th-Na) cationic space, defined by the equation Na = 1.34 + 0.81(Nb + Ta) + 0.67(REE + Y + Th).

The main compositional variations for representative rinkite and nacareniobsite-(Ce) as well as the ideal rinkite and nacareniobsite-(Ce) endmembers, are shown in Figures 5A and 5B. Below, the main exchange reac-

tions of Petersen *et al*. (1989) have been slightly modified to accommodate some minor substitutions of Ca, Nb, and Ti for other measurable cations with equivalent charges and site preferences:

$$Na + M^{5+} \leftrightarrow M^{2+} + M^{4+} \quad (1)$$

and

$$Na + (REE,Y) \leftrightarrow 2\ M^{2+} \quad (2)$$

in which equation (1) involves the A^P, $M^O{}_{(2,3)}$, and M^H, and equation (2) the A^P, $M^O{}_{(1)}$, and M^H cation sites in the structural scheme of Sokolova & Hawthorne (2008). A compilation of the existing literature data reveals poor oxide totals as well as inappropriate structural formulae for some analyses. Hence, these analyses were not considered in Figure 5.

As depicted in Figure 5A, the data align well between ideal rinkite and nacareniobsite-(Ce) endmembers with an exceptional determination coefficient $r^2 = 0.99$. This diagram supports the suggestion by Petersen *et al*. (1989) of a complete solid solution between these two minerals. 'Mosandrite' from the type locality and nacareniobsite-(Ce) from Morro Redondo, in particular, plot very close to the ideal endmembers. Their molecular compositions may be defined by $rnk_{91.6}$ $ncr_{8.4}$ and $rnk_{4.0}$ $ncr_{96.0}$, respectively, given the (Nb + Ta)/(Ti + Zr) relationships at the $M^O{}_{(1)}$ site, where rnk = rinkite and ncr = nacareniobsite. In detail, a minor shift from the endmembers join towards relatively lower bivalent and tetravalent cation totals, which is more evident in the nacareniobsite-(Ce) analyses, is inferred from Figure 5A. Of note, our data indicate also a systematic excess in REE + Y relative to the ideal value of 1 *apfu*, resulting in Na + (REE,Y) > 4 *apfu* (Fig. 5B). This evidence indicates that the incorporation of the REEs + Y into the mineral structure in high-(REE,Y) and -(Na/Ca) environments is also due to an exchange reaction of the type $[M^{+2}M^{+4}]_{-1}[(REE,Y)]_2$. A significant negative correlation between $M^{+2} + M^{+4}$ and 2(REE,Y) with $r^2 = 0.86$ (not shown) observed for our data supports such an inference. In addition, this could also explain why some of the data reported here include some minor Na excess relative to the ideal 3.0 *apfu* at the $M^O{}_{(2)}$ and the two equivalent $M^O{}_{(3)}$ sites. If this is correct, then the excess Na must fill in M^H sites (*cf*. Table 3).

Following Cámara *et al*. (2011), we have fitted the data reported here along with those presented by them

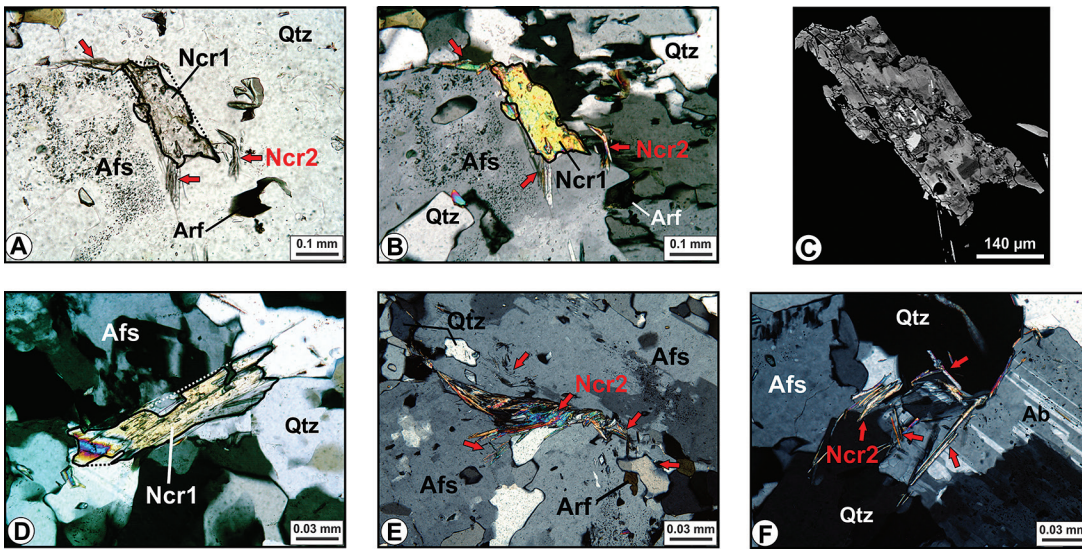

FIG. 3. Transmitted light and BSE compositional images of nacareniobsite-(Ce) from sub-magmatic deformed peralkaline alkali-feldspar granite of the Papanduva Pluton, Morro Redondo Complex. (A) Platy, subidiomorphic crystal and minor fibrous lathy crystals (red arrows), under plane polarized light. Dotted lines define the original crystal outline. Sample MR-02A. (B) Crystals depicted in A under crossed polarizers. (C) BSE image of the platy crystal depicted in A, showing typical patchy zoning and minute white internal areas of unidentified Nb-rich minerals with high atomic backscattering coefficients. (D) Prismatic, subidiomorphic crystal under plane polarized light. Dotted lines define the original crystal outline. Sample MR-140. (E) Aggregate of fibrous and minute acicular crystals (red arrows) under crossed polarizers. Sample MR-02A. (F) Idiomorphic, fibrous and acicular crystals (red arrows) under crossed polarizers. Sample MR-02. Contrasted textural generations of nacareniobsite-(Ce) – Ncr1: first generation, prismatic and Ncr2: second generation, fibrous/acicular. Qtz: quartz; Afs: alkali feldspar; Ab: albite; Arf: arfvedsonite.

TABLE 2. RARE ACCESSORY MINERALS THAT COEXIST WITH NACARENIOBSITE-(Ce) AND BRITHOLITE-(Ce) IN SAMPLES OF THE PAPANDUVA PERALKALINE GRANITE AND THEIR AVERAGE REE CONTENTS (wt.%)

Mineral	Sample					Average REE Contents		
	MR-02	MR-02A	MR-03	MR-50	MR-140	REE_2O_3	$LREE_2O_3$	$HREE_2O_3$
britholite-(Ce)			x	x		66.95	66.82	0.13
nacareniobsite-(Ce)	x	x			x	21.74	21.61	0.13
narsarsukite	x	x	x	x	x	0.56	0.03	0.53
(Na,K)-zirconosilicates*	x	x	x	x	x	3.10	0.62	2.48
REE-rich turkestanite	x	x			x	6.85	6.46	0.39
gerenite-(Y) (?)	x	x			x	14.93	6.65	8.28
kuannersuite-(Ce) (?)		x		x	x	53.66	53.22	0.44

* include elpidite and other unidentified zirconosilicate minerals.

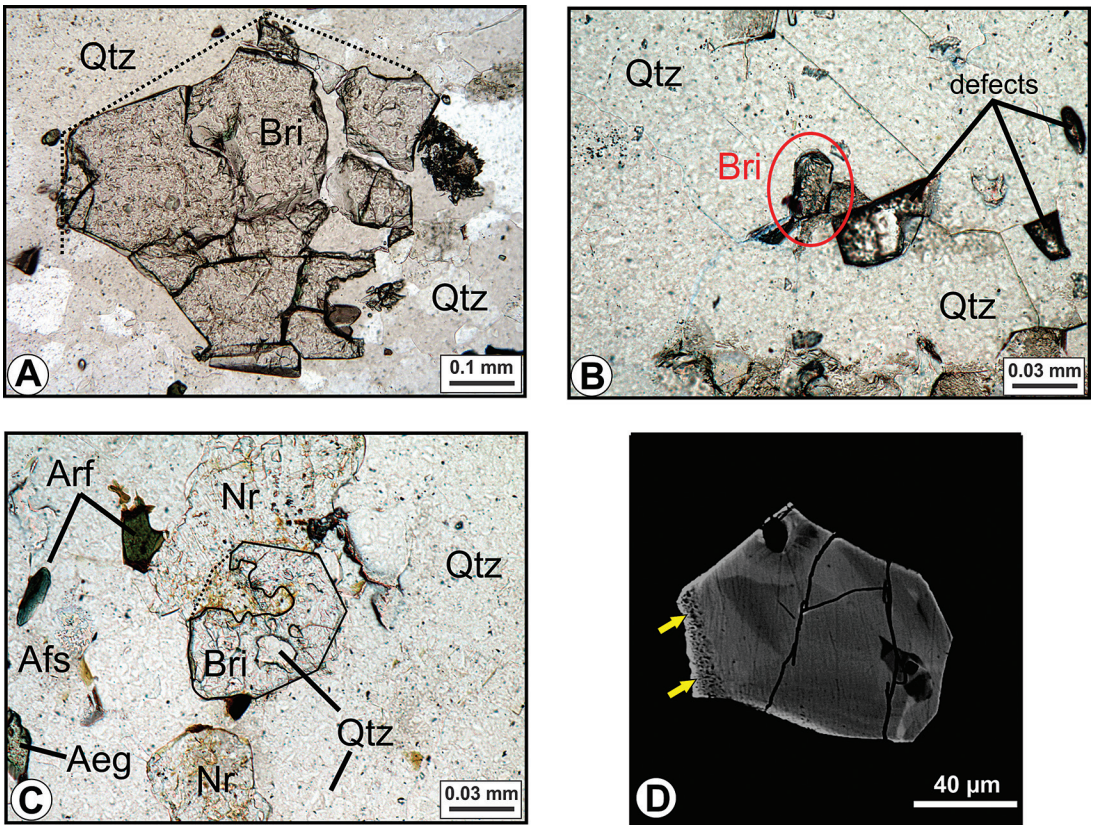

FIG. 4. Transmitted light and BSE compositional images of britholite-(Ce) from sub-magmatic deformed peralkaline alkali-feldspar granite of the Papanduva Pluton, Morro Redondo Complex. (A) Image of a near (0001) section partially broken under plane polarized light. Dotted lines partially mark the original crystal outline. Sample MR-03. (B) Small idiomorphic elongated crystal under plane polarized light. Sample MR-03. (C) Subidiomorphic crystal near basal section partially overgrowing narsarsukite. Also note quartz inclusions. Plane polarized light. Sample MR-50. (D) BSE image of a different crystal, showing zoning and spongy-textured left rim, indicated by yellow arrows, in which britholite-(Ce) is partially replaced by bastnäsite. Sample MR-03. Bri: britholite-(Ce); Qtz: quartz; Afs: alkali feldspar; Arf: arfvedsonite; Nr: narsarsukite.

into the Na-Nb,Ti-REE,Y,Th space using the Isoplot program (Ludwig 2003), assuming an arbitrary relative error of 2% in all analyses. Considering solely analyses with resulting -1 < weighted residuals < 1, 15 data points give the equation Na = 1.90 + 1.14 (Nb, Ta) – 0.03 (REE,Y,Th) (*apfu*) with superior statistical parameters [Mean Square Weighted Deviation (MSWD) = 0.2 and Probability of Fit = 1], which approaches well the equation Na = 2 + (Nb,Ta) defined by the ideal rinkite and nacareniobsite-(Ce) endmembers.

REE and trace-element patterns in nacareniobsite-(Ce)

REE + Y contents in our nacareniobsite-(Ce) vary between 21.1 and 24.9 wt.% (1.08–1.28 *apfu*) and are, in general, higher than literature data (*cf.* Table 3). REE + Y chondrite-normalized patterns are displayed in Figure 6. Our analyses are characterized by enriched concentrations of LREEs and HREEs that are up to 4.4–5 and 2–3 orders of magnitude higher, respectively, relative to those for chondrite. Figure 6A compares available partial EPMA-derived patterns for nacareniobsite-(Ce) and rinkite. The patterns reported here are in general more homogenous and exhibit a gentle concavity in the LREE region, with $La_N \leq Ce_N \leq Pr_N$, as well as a relative enrichment and depletion in the Pr-Sm and Dy-Y ranges, respectively; in particular when compared to the literature data for rinkite and 'mosandrite'. Complete REE patterns are shown in Figure 6B; these display steep, negatively sloped lines indicating small, moderate, and very high fractionations within the LREEs ($2.2 \leq Ce_N/Sm_N \leq 1.8$), of the LREEs over the MREEs ($320 \leq Ce_N/Yb_N \leq 96$), and within the HREEs ($40 \leq Dy_N/Lu_N \leq 17$), respectively; a negative Eu anomaly is typical, with Eu/Eu* [= $Eu/(Sm \times Gd)^{0.5}$] between 0.09 and 0.13. Compared to the host-rock, nacareniobsite-(Ce) is relatively enriched for the entire REE spectra, with increasing enrichment factors from the heavy- to the light-REE, with mineral/rock (m/r) ratios $2 < Lu_{N(m/r)} < 7$ and $440 < Ce_{N(m/r)} < 470$.

Partial host-rock-normalized patterns relative to the most pertinent trace elements are depicted in Figure 7. Relative to the host granite, nacareniobsite-(Ce) is

TABLE 3. REPRESENTATIVE WDS COMPOSITIONS (wt.%) AND STRUCTURAL FORMULAE FOR NACARENIOBSITE-(Ce) AND RINKITE FROM THE PAPANDUVA PERALKALINE GRANITE AND OTHER LOCALITIES TAKEN FROM THE LITERATURE

Mineral	Nacareniobsite-(Ce)												Rinkite		
Point_ID	p.1_r	p.5_i	p.7_i	p.8_c	p.9_i	p.11_i	f.2_i	f._3i	A*	B	C	D	A	E	F
SiO_2	28.34	28.44	28.28	28.43	28.14	28.31	28.15	28.33	29.63	28.30	29.54	29.00	29.18	29.36	29.78
TiO_2	0.38	0.15	0.16	0.19	0.28	0.18	0.89	0.57	2.79	2.24	1.99	2.01	5.37	8.21	8.47
ZrO_2	b.d.	b.d.	b.d.	b.d.	b.d.	0.05	0.04	b.d.	n.r.	n.r.	0.26	0.04	0.63	0.62	0.79
Al_2O_3	b.d.	b.d.	b.d.	b.d.	b.d.	0.02	0.02	b.d.	n.r.	n.r.	n.r.	0.03	n.r.	n.r.	b.d.
FeO	b.d.	b.d.	b.d.	b.d.	b.d.	b.d.	0.07	0.05	n.r.	n.r.	n.r.	n.r.	n.r.	n.r.	n.r.
MnO	b.d.	b.d.	b.d.	b.d.	b.d.	b.d.	0.02	0.02	n.r.	n.r.	0.24	n.r.	n.r.	0.13	n.r.
CaO	18.56	18.25	18.67	18.72	18.31	19.17	17.05	17.85	19.92	19.79	20.35	16.88	23.00	24.43	27.06
BaO	b.d.	0.09	b.d.	0.11	0.03	b.d.	0.08	b.d.	n.r.	n.r.	n.r.	n.r.	n.r.	0.10	n.r.
SrO	0.11	0.04	0.16	0.10	0.10	0.12	0.07	0.08	0.27	0.45	n.r.	n.r.	n.r.	1.73	0.26
Na_2O	11.10	11.06	11.00	11.10	10.92	11.07	11.03	11.00	10.01	10.07	8.29	10.57	9.38	8.37	7.59
La_2O_3	2.68	2.87	2.76	2.90	2.29	2.06	3.10	2.96	4.09	4.42	4.54	3.19	2.64	3.56	3.14
Ce_2O_3	9.55	9.73	9.54	8.81	10.00	9.13	11.59	11.02	10.32	10.55	9.19	10.34	8.62	9.00	8.36
Pr_2O_3	1.62	1.65	1.70	1.74	1.29	1.62	1.71	1.41	1.42	1.12	1.51	1.35	1.36	1.01	0.85
Nd_2O_3	6.40	6.55	6.17	6.80	5.59	6.07	5.98	5.45	4.19	4.34	3.49	5.57	5.33	3.58	2.58
Sm_2O_3	1.43	1.32	1.27	1.06	1.11	1.19	1.21	1.38	0.81	0.64	0.61	0.83	0.98	0.58	0.40
Gd_2O_3	0.77	0.97	0.52	0.41	0.78	0.63	0.65	0.64	n.r.	0.47	1.11	n.r.	n.r.	0.52	n.r.
Dy_2O_3	0.15	0.15	0.35	0.30	0.14	0.27	0.16	0.12	0.05	n.r.	n.r.	n.r.	0.03	0.41	0.30
Y_2O_3	0.22	0.15	0.31	0.34	0.21	0.35	0.53	0.44	0.78	0.57	1.76	0.48	1.07	1.83	1.79
ThO_2	b.d.	b.d.	b.d.	b.d.	0.05	b.d.	b.d.	b.d.	n.r.	n.r.	n.r.	0.03	n.r.	1.12	0.00
Nb_2O_5	14.92	15.20	15.47	15.15	14.94	15.30	14.00	14.51	11.61	12.01	9.42	12.03	6.63	1.89	1.34
Ta_2O_5	0.53	0.43	0.35	0.48	0.35	0.52	0.60	0.67	0.34	0.33	n.r.	n.r.	0.26	n.r.	0.07
F	6.43	6.35	6.79	6.73	6.52	6.53	6.02	5.91	6.87	6.15	5.62	6.22	6.57	6.47	7.48
O=F	2.71	2.67	2.86	2.83	2.75	2.75	2.53	2.49	2.89	2.59	2.37	2.62	2.77	2.72	3.15
Total	100.50	100.74	100.65	100.57	98.30	99.86	100.42	99.93	100.21	98.86	95.55	95.95	98.28	100.20	97.11

TABLE 3 CONT. *Structural Formulae [(O+F) = 18 apfu]*

Mineral	Nacareniobsite-(Ce)												Rinkite		
Point_ID	p.1r	p.5i	p.7i	p.8c	p.9i	p.11i	f.2i	f.3i	A*	B	C	D	A	E	F
Si	3.993	4.010	3.966	3.987	4.017	3.984	4.015	4.034	4.075	4.014	4.273	4.180	4.040	4.016	4.033
Al	0.000	0.000	0.000	0.000	0.000	0.003	0.003	0.000	0.000	0.000	0.000	0.005	0.000	0.000	0.000
T_site	3.993	4.010	3.966	3.987	4.017	3.987	4.017	4.034	4.075	4.014	4.273	4.185	4.040	4.016	4.033
Nb	0.950	0.969	0.981	0.961	0.964	0.973	0.903	0.934	0.722	0.770	0.616	0.784	0.415	0.117	0.082
Ta	0.020	0.016	0.013	0.018	0.014	0.020	0.023	0.026	0.013	0.013	0.000	0.000	0.010	0.000	0.003
Ti	0.040	0.016	0.017	0.020	0.030	0.019	0.095	0.061	0.289	0.239	0.216	0.218	0.559	0.845	0.863
Zr	0.000	0.000	0.000	0.000	0.000	0.004	0.003	0.000	0.000	0.000	0.018	0.003	0.043	0.041	0.052
$M^{O}(1)$_site	1.011	1.002	1.011	0.998	1.008	1.016	1.024	1.021	1.023	1.022	0.851	1.005	1.026	1.003	0.999
Na	3.008	2.983	2.962	2.986	2.944	3.012	2.975	3.000	2.669	2.769	2.325	2.713	2.518	2.220	1.993
Ca	0.000	0.000	0.000	0.000	0.000	0.000	0.000	0.000	0.058	0.197	0.391	0.000	0.442	0.831	0.845
$M^{O}(2,3)$_site	3.008	2.983	2.962	2.986	2.944	3.012	2.975	3.000	2.727	2.966	2.717	2.713	2.960	3.051	2.838
Na	0.024	0.041	0.029	0.032	0.079	0.009	0.075	0.044	0.000	0.000	0.000	0.241	0.000	0.000	0.000
Ca	2.802	2.757	2.806	2.813	2.801	2.891	2.605	2.723	2.877	2.810	2.763	2.607	2.969	2.750	3.081
FeII	0.000	0.000	0.000	0.000	0.000	0.000	0.008	0.006	0.000	0.000	0.000	0.000	0.000	0.000	0.000
Mn	0.000	0.000	0.000	0.000	0.000	0.000	0.003	0.002	0.000	0.000	0.029	0.000	0.000	0.015	0.000
Ba	0.000	0.005	0.000	0.006	0.002	0.000	0.004	0.000	0.000	0.000	0.000	0.000	0.000	0.005	0.000
Sr	0.009	0.003	0.013	0.008	0.008	0.010	0.005	0.007	0.022	0.037	0.000	0.000	0.000	0.137	0.020
$M^{(+1,+2)}$_site	2.834	2.806	2.848	2.859	2.889	2.909	2.701	2.782	2.898	2.847	2.792	2.848	2.969	2.907	3.101
Dy	0.007	0.007	0.016	0.014	0.006	0.012	0.007	0.005	0.002	0.000	0.000	0.000	0.001	0.018	0.013
Gd	0.036	0.045	0.024	0.019	0.037	0.029	0.031	0.030	0.000	0.022	0.053	0.000	0.000	0.024	0.000
Sm	0.069	0.064	0.061	0.051	0.055	0.058	0.059	0.068	0.038	0.031	0.030	0.041	0.047	0.027	0.019
Nd	0.322	0.330	0.309	0.340	0.285	0.305	0.305	0.277	0.206	0.220	0.180	0.287	0.264	0.175	0.125
Pr	0.083	0.085	0.087	0.089	0.067	0.083	0.089	0.073	0.071	0.058	0.080	0.071	0.069	0.050	0.042
Ce	0.493	0.502	0.490	0.452	0.523	0.470	0.605	0.574	0.520	0.548	0.487	0.546	0.437	0.451	0.414
La	0.139	0.149	0.143	0.150	0.121	0.107	0.163	0.156	0.207	0.231	0.242	0.170	0.135	0.180	0.157
Y	0.016	0.011	0.023	0.025	0.016	0.026	0.040	0.034	0.057	0.043	0.135	0.037	0.079	0.133	0.129
Th	0.000	0.000	0.000	0.000	0.002	0.000	0.000	0.000	0.000	0.000	0.000	0.001	0.000	0.035	0.000
$M^{(+3,+4)}$_site	1.166	1.194	1.152	1.141	1.111	1.091	1.299	1.217	1.102	1.153	1.208	1.152	1.031	1.093	0.899
(M^{H},A^{P})	4.000	4.000	4.000	4.000	4.000	4.000	4.000	4.000	4.000	4.000	4.000	4.000	4.000	4.000	4.000
Cations	12.012	11.995	11.939	11.972	11.969	12.014	12.016	12.045	11.825	12.002	11.841	11.903	12.027	12.069	11.871
O	15.135	15.168	14.988	15.015	15.056	15.095	15.287	15.339	15.012	15.241	15.429	15.164	15.123	15.201	14.796
F	2.865	2.832	3.012	2.985	2.944	2.905	2.713	2.661	2.988	2.759	2.571	2.836	2.877	2.799	3.204

Structural formulae computed following Sokolova & Hawthorne (2008). Point_ID: crystal/spot identification, p: platy crystal, f: fibrous, c: core, i: intermediate, r: rim (our data, sample MR-02). Other analyses: A: Petersen *et al.* (1989), B: Sokolova & Hawthorne (2008), C: Ridolfi *et al.* (2006), D: Pekov & Ekimenkova (2001), E: Cámara *et al.* (2011), F: 'mosandrite' (Sokolova & Cámara 2008). (*): mean analyses. b.d.: below detection limit, n.r.: not reported

enriched, besides in the REEs, in Sr (up to 2.9 orders of magnitude), and depleted in alkali metals, in particular Rb and Zr. Abundances of the remaining elements are similar, with relative enrichment or depletion within ~1.5 orders of magnitude.

Unidentified Nb-rich mineral in nacareniobsite-(Ce)

As stated above, typical nacareniobsite-(Ce) crystals contain minute internal areas that were problematical for WDS analyses, with higher BSE signals (Fig. 3C), corresponding to unidentified Nb-rich minerals. Compared to EDS patterns for nacareniobsite-(Ce), those for the unidentified phases contain higher Nb (up to 2-fold) and lower Si (up to 0.5-fold), Ca (0.5-fold) and REEs, and similar Na uncorrected intensities. The chemical nature of these areas (with the exception of their relative elemental intensities) are very similar to those described by Petersen *et al.* (1989) for nacareniobsite-(Ce) from the Ilímaussaq Complex and attributed to Na- and Ca-leaching due to late alteration processes. In our case, however, these areas are not depleted in Na to a significant extent nor significantly enriched in REEs.

Britholite-(Ce)

Britholite-(Ce) and the REE-fluorcarbonate bastnäsite, which occurs as a replacement product in the studied samples and also as independent crystals in other samples (Vilalva 2007), along with an as-yet poorly studied REE-silicophosphate [probably kuannersuite-(Ce)], are the most (REE,Y)-enriched minerals

in the peralkaline granites from the Morro Redondo Complex (Table 2). The britholite-(Ce) is classified as britholite *senso strictu*, with ∑(REE,Y) > Ca (Pekov *et al*. 2007). (REE,Y) contents are among the highest reported to date, up to 73.6 wt.% oxide (9.98 *apfu*). SiO_2 and Na_2O abundances are also relatively high, whereas P_2O_5 and CaO contents are low. Fluorine contents vary from 1.45 to 2.63 wt.%, and some of these analyses, in addition to literature data (*cf.* analyses 3_r, D* and E* in Table 5), may actually be classified as fluorbritholite (Gu *et al*. 1994). Of note, structural formulae computed on the basis of 26 (O,F) indicate a minor systematic deficit in the tetrahedral sites with *ca*. 5.80 ≤ (Si + P) ≤ 5.97 *apfu* (*cf.* Table 5). On the basis of the study by Oberti *et al*. (2001), such deficiencies may be indicative of unanalyzed B within these structural positions.

The main compositional variations observed in the britholite series are analogous to those observed in the apatite supergroup, and may be attributed to the $[PM^{2+}]_{-1}[Si(REE,Y)]$ and $[M^{2+}]_{-2}[Na(REE,Y)]$ coupled substitution mechanisms (*e.g*., Rønsbo 1989, Kalsbeek *et al*. 1990, Fleet & Pan 1995, Chang *et al*. 1998, Oberti *et al*. 2001, Pan & Fleet 2002, Chen & Simonetti *in press*). The compositions reported here and those compiled from the literature are evaluated on the basis of these substitution schemes (Fig. 8). The trends shown in Figure 8 clearly demonstrate the effectiveness of both mechanisms, since these define high determination coefficients ($r^2 \geq 0.98$). As expected, compositional data obtained here plot in areas with the highest [Si + (REE,Y)] and [Na + (REE,Y)] contents, well beyond the ideal britholite-(Ce) endmember. Importantly, our EPMA data also reveal a relatively good positive correlation between P and F contents (not shown), which suggests a more general substitution mechanism for the first scheme to include the coupled $[OH]_{-1}F$, such as:

$$Si + (REE,Y) + (OH) \leftrightarrow P + M^{2+} + F \quad (3)$$

TABLE 4. REPRESENTATIVE TRACE-ELEMENT LA-ICP-MS DATA FOR NACARENIOBSITE-(Ce) FROM THE PAPANDUVA PERALKALINE GRANITE (SAMPLE MR-02)

Mineral	Nacareniobsite-(Ce)											
Point_ID	2.1		2.2		3.1		3.2		5.1		5.2	
	ppm	2σ	ppm	2σ	ppm	2σ	ppm	2σ	ppm	2σ	ppm	2σ
Li	8.7	0.9	9.6	0.9	b.d.		8.6	0.9	7.4	0.8	8.2	0.9
Sc	1.1	0.2	1.3	0.2	3.9	0.7	1.1	0.2	0.6	0.1	1.7	0.2
Mn	8.4	0.6	31.3	2.0	5.8	0.9	7.9	0.6	9.7	0.7	17.3	1.1
Co	0.27	0.06	0.20	0.06	0.30	0.22	0.28	0.06	0.18	0.07	1.77	0.15
Cu	0.40	0.09	0.61	0.11	4.29	0.78	0.41	0.09	0.26	0.09	0.27	0.09
Zn	85	5	91	6	90	7	90	6	75	5	83	5
Ga	38	2	40	2	80	5	38	2	32	2	33	2
Rb	0.9	0.1	1.1	0.1	0.9	0.2	0.7	0.1	1.4	0.1	3.5	0.2
Sr	635	39	637	39	756	50	655	40	624	39	666	41
Zr	18	1	49	3	256	19	29	2	10	1	52	4
Sn	3.4	0.4	2.9	0.4	6.4	1.4	2.9	0.4	2.0	0.4	3.1	0.4
Cs	1.21	0.09	1.16	0.08	1.12	0.15	1.12	0.08	1.1	0.1	3.2	0.2
Ba	249	15	253	15	191	12	250	15	196	12	209	13
Nd	52143	3192	56570	3467	50722	3187	60122	3691	43564	2661	46416	2835
Sm	8956	548	9525	583	11940	750	9828	602	9338	572	10133	621
Eu	257	16	277	17	277	18	284	17	271	17	274	17
Gd	5451	334	5348	328	6806	428	5711	350	5717	351	6039	371
Tb	617	38	681	42	617	39	681	42	697	43	697	43
Dy	2420	149	2695	166	1878	119	2703	167	2759	170	2610	161
Ho	296	18	342	21	177	11	334	21	361	22	332	21
Er	581	36	677	42	315	20	651	40	679	42	625	39
Tm	40	3	51	3	16	1	49	3	46	3	45	3
Yb	170	11	222	14	66	5	210	13	174	11	191	12
Lu	11.3	0.7	15.6	1.0	4.6	0.5	15.0	0.9	11.4	0.7	13.8	0.9
Hf	4.8	0.3	6.2	0.4	5.7	0.7	5.3	0.4	2.3	0.2	12.2	0.8
Ta	b.d.		b.d.		4183	269	b.d.		b.d.		56.6	3.6
Pb	13.1	0.8	14.0	0.9	8.1	0.9	15.3	1.0	22.4	1.4	26.3	1.7
Th	33.4	2.1	46.8	2.9	4.3	0.5	41.6	2.6	7.7	0.5	17.9	1.2
U	26.4	1.6	25.4	1.5	11.5	0.8	23.8	1.5	26.7	1.6	21.5	1.3

Point_ID = crystal/spot identification. Deviations (2σ) are given in absolute values for a 95% confidence level. V, Cr, and Ni, close or below the detection limit, were omitted; La, Ce, Pr, and Y were not analyzed. b.d.: below detection limit.

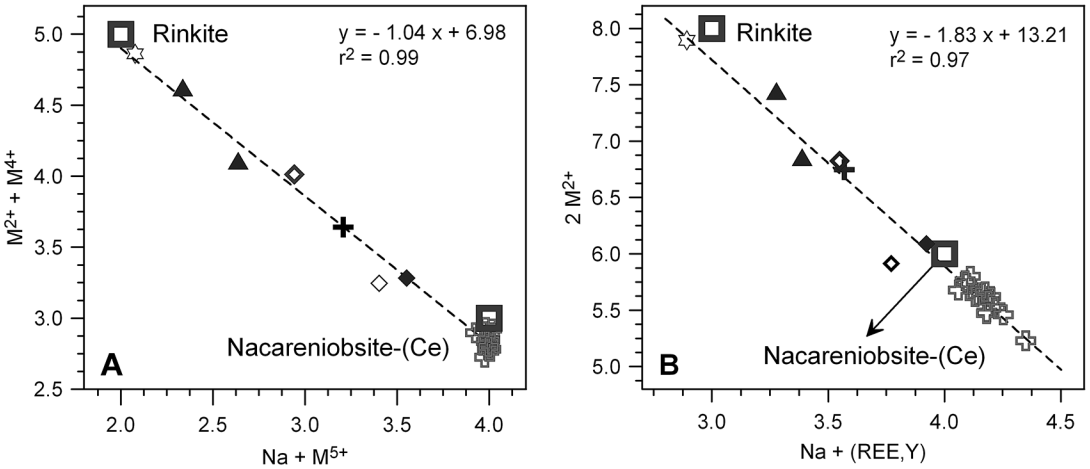

FIG. 5. Representative compositions of rinkite and nacareniobsite-(Ce) in cationic diagrams. (A) $M^{2+} + M^{4+}$ *versus* $Na + M^{5+}$ and (B) $2M^{2+}$ *versus* Na + (REE,Y). The ideal rinkite and nacareniobsite-(Ce) endmembers are plotted as open squares. Note the exceptional correlation of the available data in both diagrams and Na + (REE,Y) values in our samples higher than the ideal nacareniobsite-(Ce). Symbols: stars: "mosandrite" from the type locality (Sokolova & Cámara 2008); full triangles: Cámara *et al*. (2011); open diamonds [heavy: rinkite, light: nacareniobsite-(Ce)], Petersen *et al*. (1989); crosses, Ridolfi *et al*. (2006); filled diamond, (Sokolova & Hawthorne 2008); light open crosses: this work.

TABLE 5. REPRESENTATIVE WDS COMPOSITIONS AND STRUCTURAL FORMULAE FOR BRITHOLITE-(Ce) FROM THE PAPANDUVA PERALKALINE GRANITE AND OTHER LOCALITIES TAKEN FROM LITERATURE

Mineral	Britholite-(Ce)														
Point_ID	1_i	2_i	1_c	2_c	2_i	2i	2_r	3_c	3_r	A	B*	C*	D*	E*	F
SiO_2	19.39	19.46	19.77	20.29	20.01	20.23	20.13	19.94	19.50	21.10	17.10	20.89	19.56	16.20	20.51
ThO_2	0.24	0.31	0.31	0.15	0.19	0.26	0.31	b.d.	0.27	11.92	n.r.	20.73	1.12	n.r.	1.88
UO_2	0.02	b.d.	b.d.	0.05	b.d.	b.d.	0.10	b.d.	b.d.	2.12	n.r.	1.47	0.78	n.r.	0.30
Al_2O_3	b.d.	0.02	b.d.	b.d.	b.d.	b.d.	b.d.	b.d.	b.d.	0.00	n.r.	n.r.	n.r.	0.09	0.88
La_2O_3	15.28	13.95	15.76	16.70	16.49	17.79	16.96	17.32	14.90	11.23	17.98	7.35	8.67	16.30	13.28
Ce_2O_3	32.15	32.62	32.64	32.02	33.87	31.56	31.89	31.80	33.77	21.70	29.42	18.61	25.48	22.50	24.03
Pr_2O_3	3.75	4.14	3.17	3.78	3.58	3.60	3.88	2.98	3.65	2.19	2.48	1.64	n.r.	2.79	n.r.
Nd_2O_3	14.36	13.65	13.57	13.41	13.46	14.15	13.89	14.20	13.21	5.92	7.55	5.10	13.62	6.92	4.63
Sm_2O_3	2.56	1.92	2.07	2.00	2.28	2.20	2.47	2.30	2.25	0.72	n.r.	n.r.	2.02	1.66	n.r.
Gd_2O_3	1.38	1.30	1.72	1.42	1.80	1.89	1.69	2.07	0.89	0.50	n.r.	n.r.	1.27	2.85	n.r.
Dy_2O_3	0.41	0.69	0.43	0.78	0.63	0.59	0.50	0.44	0.34	0.31	n.r.	n.r.	0.54	0.29	n.r.
Yb_2O_3	0.04	b.d.	0.12	0.15	0.08	b.d.	0.04	0.10	0.05	0.12	n.r.	n.r.	n.r.	0.18	n.r.
Y_2O_3	1.34	1.23	1.38	1.49	1.44	1.43	1.38	1.71	0.72	1.71	n.r.	n.r.	2.07	0.40	1.08
FeO	0.15	0.12	0.10	0.03	b.d.	0.05	0.08	b.d.	0.13	0.00	n.r.	n.r.	n.r.	n.r.	0.00
MnO	0.05	0.11	0.06	0.02	0.08	0.05	0.14	0.15	0.22	0.00	n.r.	n.r.	n.r.	n.r.	n.r.
MgO	b.d.	b.d.	b.d.	b.d.	b.d.	b.d.	b.d.	b.d.	b.d.	0.00	n.r.	n.r.	n.r.	0.02	n.r.
CaO	3.58	4.39	3.74	3.28	3.34	3.27	3.33	3.50	4.61	16.80	11.93	19.92	14.56	16.60	24.03
BaO	0.15	0.04	0.04	b.d.	b.d.	b.d.	b.d.	0.05	0.10	0.00	0.00	n.r.	n.r.	n.r.	n.r.
Na_2O	2.11	2.32	2.05	1.66	1.66	1.71	1.66	1.92	1.76	0.00	1.91	n.r.	n.r.	n.r.	0.74
P_2O_5	1.09	2.01	1.28	0.16	0.20	0.12	0.20	0.20	1.18	1.11	8.07	4.30	2.94	7.03	8.19
F	1.90	2.14	2.04	1.69	1.45	1.51	1.73	2.20	2.39	2.12	0.00	n.r.	2.99	3.80	2.52
O=F	0.95	1.07	1.02	0.85	0.72	0.75	0.87	1.10	1.20	1.06	0.00	n.r.	1.49	1.90	1.06
Total	99.00	99.36	99.23	98.23	99.84	99.67	99.52	99.81	98.74	98.51	96.44	100.01	94.10	95.73	96.72

TABLE 5 CONT. *Structural formulae [26 (O,F) apfu]*

Point_ID	1_i	2_i	1_c	2_c	2_i	2i	2_r	3_c	3_r	A	B*	C*	D*	E*	F
Si	5.607	5.487	5.651	5.923	5.800	5.860	5.841	5.784	5.615	5.635	4.388	5.211	5.347	4.278	4.663
P	0.266	0.480	0.310	0.040	0.050	0.030	0.048	0.050	0.287	0.251	1.753	0.908	0.679	1.572	1.577
T_site	5.873	5.967	5.961	5.964	5.850	5.890	5.889	5.834	5.902	5.886	6.142	6.119	6.026	5.849	6.240
Th	0.016	0.020	0.020	0.010	0.013	0.017	0.020	0.000	0.018	0.724	0.000	1.177	0.070	0.000	0.097
U	0.001	0.000	0.000	0.003	0.000	0.000	0.007	0.000	0.000	0.126	0.000	0.082	0.047	0.000	0.015
Al	0.000	0.005	0.000	0.000	0.000	0.000	0.000	0.000	0.000	0.000	0.000	0.000	0.000	0.028	0.236
La	1.629	1.450	1.661	1.798	1.762	1.900	1.815	1.853	1.582	1.106	1.702	0.676	0.874	1.587	1.114
Ce	3.404	3.367	3.415	3.423	3.594	3.347	3.389	3.377	3.560	2.122	2.764	1.699	2.550	2.175	2.000
Pr	0.395	0.426	0.330	0.402	0.378	0.379	0.410	0.315	0.383	0.213	0.232	0.149	0.000	0.268	0.000
Nd	1.483	1.374	1.385	1.399	1.393	1.463	1.440	1.471	1.358	0.565	0.692	0.454	1.329	0.653	0.376
Sm	0.256	0.187	0.204	0.201	0.227	0.219	0.247	0.230	0.223	0.066	0.000	0.000	0.191	0.151	0.000
Gd	0.132	0.121	0.163	0.137	0.173	0.182	0.162	0.199	0.085	0.044	0.000	0.000	0.115	0.249	0.000
Dy	0.038	0.062	0.039	0.073	0.059	0.055	0.046	0.041	0.031	0.027	0.000	0.000	0.048	0.025	0.000
Yb	0.004	0.000	0.011	0.013	0.007	0.001	0.003	0.009	0.004	0.010	0.000	0.000	0.000	0.014	0.000
Y	0.206	0.184	0.211	0.232	0.222	0.220	0.213	0.264	0.111	0.243	0.000	0.000	0.302	0.056	0.131
Fe	0.037	0.029	0.023	0.008	0.000	0.012	0.020	0.000	0.032	0.000	0.000	0.000	0.000	0.000	0.000
Mn	0.012	0.027	0.015	0.004	0.018	0.011	0.034	0.036	0.055	0.000	0.000	0.000	0.000	0.000	0.000
Mg	0.000	0.000	0.000	0.000	0.000	0.000	0.000	0.000	0.000	0.000	0.000	0.000	0.000	0.008	0.000
Ca	1.109	1.326	1.145	1.025	1.038	1.016	1.036	1.087	1.423	4.807	3.280	5.324	4.264	4.696	4.681
Ba	0.017	0.005	0.004	0.000	0.000	0.000	0.000	0.006	0.011	0.000	0.000	0.000	0.000	0.000	0.000
Na	1.183	1.268	1.137	0.940	0.933	0.961	0.933	1.080	0.982	0.000	0.950	0.000	0.000	0.000	0.326
REE_site	9.921	9.851	9.762	9.670	9.819	9.785	9.775	9.969	9.857	10.054	9.620	9.561	9.788	9.912	8.976
Cations	15.795	15.819	15.723	15.634	15.670	15.674	15.664	15.802	15.759	15.940	15.762	15.680	15.814	15.761	15.216
O	24.259	24.089	24.160	24.437	24.675	24.619	24.412	23.979	23.820	24.209	26.000	26.000	23.419	22.827	24.191
F	1.741	1.911	1.840	1.563	1.325	1.381	1.588	2.021	2.180	1.791	0.000	0.000	2.581	3.173	1.809

Structural formulae computed following Oberti et al. (2001). Point_ID: crystal/spot identification, c: core, r: rim, i: intermediate (our data, sample MR-03). Other analyses: A: Oberti *et al.* (2001), B: Kalsbeek *et al.* (1990), C: Orlandi *et al.* (1989), D: Arden & Halden (1999), E: Nash (1972), F: Melluso *et al.* (2012) (*): mean analyses. b.d.: below detection limit, n.r.: not reported.

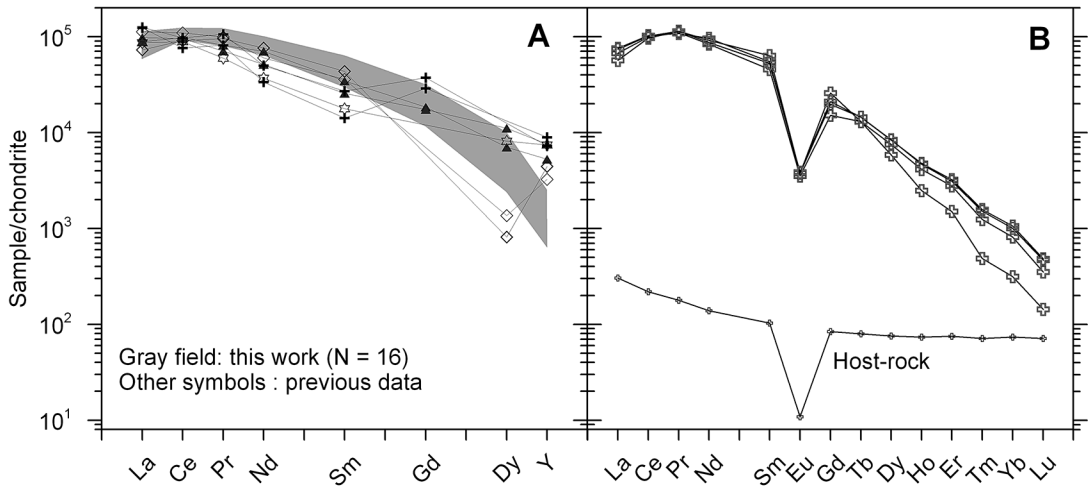

FIG. 6. Representative rinkite and nacareniobsite-(Ce) REE patterns, normalized after Boynton (1984). (A) Partial EPMA data, symbols as in Figure 3, except for our data, represented by the grayish field. (B) Complete, combined EPMA-LA-ICP-MS patterns for nacareniobsite-(Ce) from the Papanduva peralkaline granite to which the whole-rock pattern for the host sample (sample MR-02) is added for comparison.

TABLE 6. REPRESENTATIVE LA-ICP-MS TRACE-ELEMENT ABUNDANCES FOR BRITHOLITE-(Ce) FROM THE PAPANDUVA PERALKALINE GRANITE (SAMPLE MR-03)

Mineral	Britholite-(Ce)											
Point_ID	1.1.		1.2		2.1		2.2		1.3		2.3	
Element	ppm	2σ	ppm	2σ	ppm	2σ	ppm	2σ	ppm	2σ	ppm	2σ
Be	b.d.		b.d.		b.d.		b.d.		1.4	1.1	b.d.	
Mn	354	37	413	43	399	42	433	46	286	58	322	65
Ga	81	10	82	10	85	10	95	12	86	6	94	6
Rb	b.d.		1.0	0.2	0.5	0.3	1.1	0.3	0.8	0.2	0.6	0.1
Sr	1208	683	1628	920	1221	691	1139	644	3379	7859	3192	7425
Zr	b.d.		b.d.		0.8	0.4	0.5	0.4	b.d.		b.d.	
Nb	8	1	15	2	16	2	18	2	11	1	12	1
Sn	b.d.		b.d.		b.d.		b.d.		b.d.		b.d.	
Ba	602	57	615	59	640	61	692	66	471	80	473	81
Sm	9477	1141	11441	1378	11853	1431	12181	1472	7741	489	8676	551
Eu	260	24	330	30	322	30	329	30	222	37	269	44
Gd	5326	346	7708	500	8765	574	8593	565	4281	502	5794	680
Tb	546	36	801	53	786	53	768	52	491	33	609	42
Dy	2372	247	3736	389	3272	342	3250	340	2409	194	2204	178
Ho	286	28	469	47	408	41	393	39	379	40	331	35
Er	522	34	871	56	724	47	717	47	710	78	571	63
Tm	41	4	73	6	58	5	58	5	56	4	51	3
Yb	168	18	293	30	249	26	244	26	238	20	219	19
Lu	12.2	1.0	22.2	1.8	19.7	1.6	19.1	1.6	16.5	1.1	15.8	1.1
Hf	b.d.		b.d.		b.d.		0.2	0.1	0.3	0.1	0.2	0.1
Ta	b.d.		b.d.		b.d.		b.d.		b.d.		b.d.	
Pb	1714	213	1858	230	1849	230	2032	253	1184	160	1409	190
Th	1020	67	1531	101	1170	78	1297	87	965	75	873	68
U	67	8	82	9	59	7	61	7	66	13	46	9

Point_ID = crystal/spot identification. Deviations (2σ) are given in absolute values for a 95% confidence level. Li, Mg, Sc, Cr, Co, Ni, and Cu, with abundances close or below the detection limit, were omitted; La, Ce, Pr, Nd, and Y were not analyzed.

Thorium and U are not significant constituents in the britholite-(Ce) investigated here, albeit ThO_2 and/or UO_2 contents reported in literature data may be very high, up to 20.7 and 1.5 wt.% (*cf.* Table 5, analysis A* and C*), respectively. The incorporation of both elements in britholite-(Ce) and apatite, amongst others, may be accommodated by the $[M^{2+}(REE,Y)]_{-1}[Na(Th,U)]$ and $[M^{2+}(Th,U)]_{-1}[(REE,Y)]_2$ coupled substitution schemes (see Pan & Fleet 2002). The data presented here suggest that the second substitution mechanism is the most important in britholite-(Ce) (Fig. 9).

REE and trace-element patterns in britholite-(Ce)

Chondrite-normalized REE and expanded trace element host-rock-normalized patterns for britholite-(Ce) are displayed in Figures 10 and 11; Figure 10A also displays representative literature data for britholite-(Ce). With the exception of two samples from previous studies that contain higher La and similar Ce contents, the britholite-(Ce) from the Morro Redondo Complex

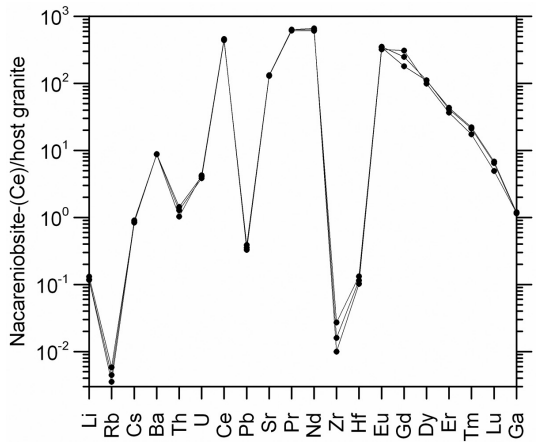

FIG. 7. Representative multi-element patterns for nacareniobsite-(Ce) from the Papanduva peralkaline granite, as normalized to the host rock (sample MR-02).

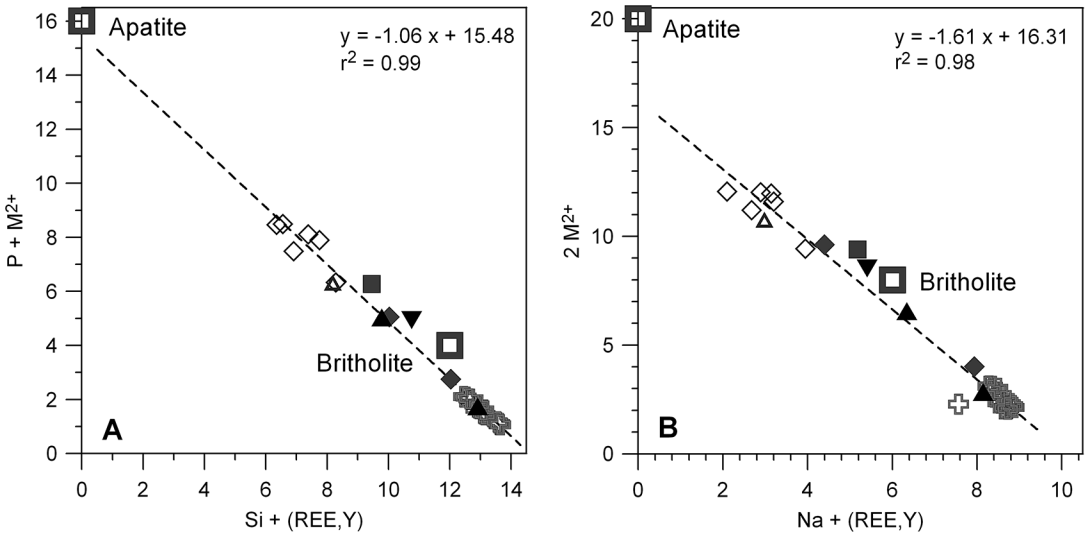

FIG. 8. Representative compositions of britholite-(Ce) in the cationic diagrams (A) P + M^{2+} *versus* Si + (REE,Y) and (B) $2M^{2+}$ *versus* Na + (REE,Y). Ideal apatite and britholite-(Ce) [$(REE,Y)_3Ca_2][(SiO_4)_3](OH,F)$] endmembers are represented by open squares. Symbols: triangles up, Kalsbeek *et al.* (1990); open diamonds, Melluso *et al.* (2012); full light diamonds, Oberti *et al.* (2001); open triangle up, Orlandi *et al.* (1989), triangle down, Arden & Halden (1999); square, Nash (1972); light open crosses, this work.

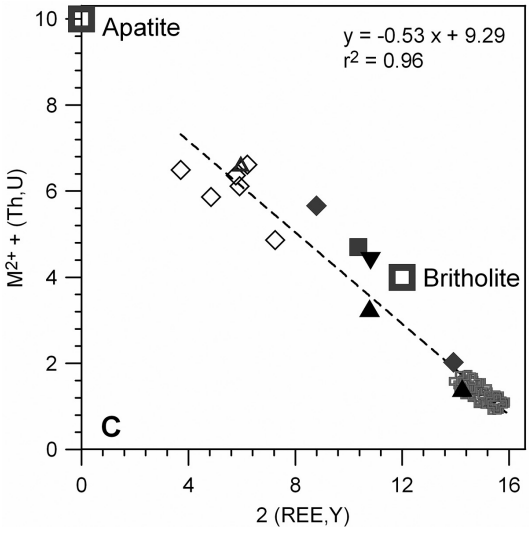

FIG. 9. Representative compositions of britholite-(Ce) in the cationic diagram M^{2+} + (Th,U) *versus* 2 (REE,Y). Symbols as in Figure 8.

is, overall, more enriched in the remaining REEs and defines smooth negatively sloped patterns (Fig. 10B). Combined EPMA–LA-ICP-MS patterns (Fig. 10A) show high fractionation values of the LREE over the HREE as well as within the LREEs and the HREEs, with $160 \leq La_N/Yb_N \leq 1800$, $4 \leq La_N/Sm_N \leq 54$, and $12 \leq Dy_N/Lu_N \leq 22$. As with nacareniobsite-(Ce), britholite-(Ce) is also characterized by a negative Eu anomaly with $0.06 \leq Eu/Eu^* \leq 0.24$. The data set reported here suggests two compositional groups, discriminated by their Dy and especially Y contents. In general, the Y-richest compositions are typical of crystal cores or intermediate zones, and therefore it may be concluded that britholite-(Ce) evolved to relatively (HREE, Y)-poor compositions as crystallization proceeded (*cf.* Table 4, spots 3_c, 3_i and 3_r, and Fig. 10A). Relative to the host granite, britholite-Ce shows significant relative enrichment in the entire REE spectra, with factors greater than those observed in nacareniobsite-(Ce), as well as for Sr; depletions in Rb, Zr and Hf, and minor relative enrichments in Ba, Th, U and Pb, up to 1.3 orders of magnitude (Fig. 11).

In general, phosphate minerals, in particular monazite and xenotime, may be considered excellent U-Th-Pb chronometers (*e.g.*, Harrison *et al.* 2002). Of interest, the measured Pb contents in our britholite-(Ce) analyses exceed to a significant degree the expected abundances generated by Th and U radioactive decay (given its Neoproterozoic age), thus implying that britholite-(Ce) may contain a significant amount of common Pb.

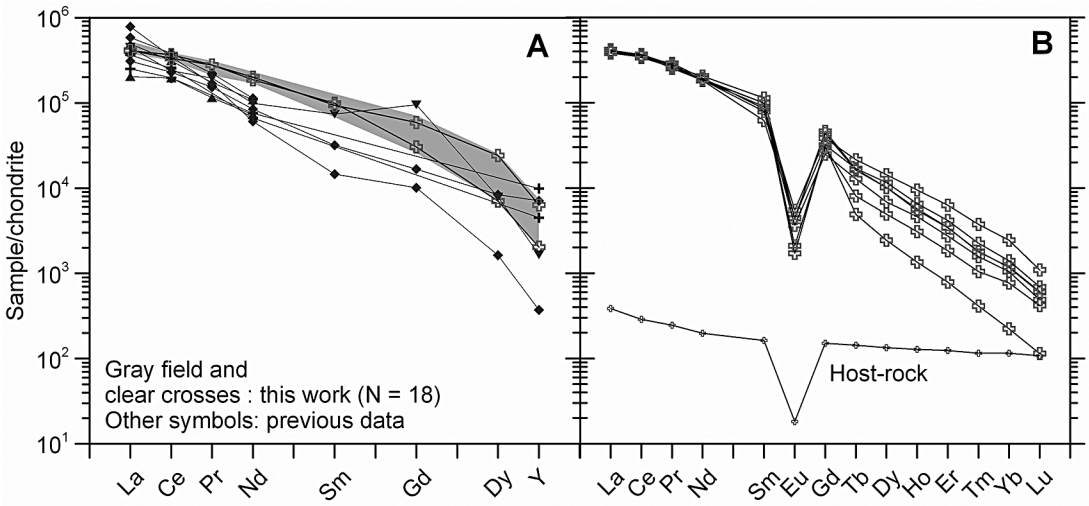

FIG. 10. Representative britholite-(Ce) REE patterns, normalized after Boynton (1984). (A) Partial EPMA data, symbols as in Figure 8 except for our samples, represented by the light grayish field. Two, among our samples, representative of relatively Y-rich and Y-poor rim and core spots from a single crystal respectively are emphasized with open crosses. (B) Complete, combined EPMA-LA-ICP-MS patterns for britholite-(Ce) from the Papanduva peralkaline granite to which the whole-rock pattern for the host sample (sample MR-03) is added for comparison.

CONCLUSIONS AND FINAL REMARKS

Nacareniobsite-(Ce) and britholite-(Ce), rare REE-bearing accessory minerals, were identified in sub-magmatic deformed peralkaline alkali-feldspar granites of the Papanduva Pluton, Graciosa Province, southern Brazil. These minerals form small sub- to idiomorphic isolated crystals in a fine-grained, saccharoidal, quartz-ofeldspathic matrix, coexisting with other rare, agpaitic accessory minerals, including narsarsukite, REE-rich turkestanite, elpidite, and other (Na,K)-zirconosilicates, and to date poorly characterized and/or unidentified phases. Furthermore, a second distinct, late-crystallizing, textural generation of nacareniobsite-(Ce) forms aggregates of fibrous and minute acicular crystals.

Textural features indicate that most of the britholite-(Ce) crystals were formed before close-to-solidus deformational episodes, since these appear systematically broken. This type of evidence is not so apparent for nacareniobsite-(Ce), since many crystals appear to have formed after deformation, especially those forming fibrous and acicular aggregates and minute laths. In any case, it is plausible to assume that deformation had driven intense circulation of residual melts and late fluids, which precipitated most of the rare minerals observed in the Papanduva peralkaline deformed granites (Vilalva & Vlach 2010).

Chemical compositions obtained for both nacareniobsite-(Ce) and britholite-(Ce) reveal that these minerals are important in controlling the REE (mainly LREE) budgets of the Papanduva peralkaline granites, along with a (Na,Ba)-rich silicophosphate, tentatively identified as kuannersuite-(Ce), that coexists with both nacareniobsite-(Ce) and britholite-(Ce) (Table 2). On the other hand, the most important minerals in controlling HREE budgets in these rocks are elpidite and other (Na,K)-zirconosilicates, as well as a yet poorly characterized Y-bearing silicate, here tentatively identified as

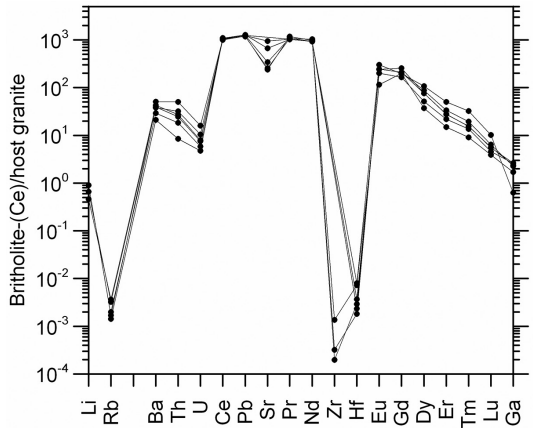

FIG. 11. Representative multi-element patterns for britholite-(Ce) from the Papanduva peralkaline granite, as normalized to the host rock (sample MR-03).

gerenite-(Y), associated with REE-rich turkestanite, as described by Vilalva & Vlach (2010, see also Table 2). Further structural and compositional studies of these minerals are being conducted.

Crystallization environment

As with other plutons from the alkaline and aluminous associations of the Graciosa A-type Province (*e.g.*, Vlach & Gualda 2007), the emplacement of the peralkaline granites of the Papanduva Pluton occurred at relatively high crustal levels, at pressures <2 kbar (Vilalva & Vlach 2013). The temperature ranges of crystallization for the peralkaline melts are difficult to assess, as pertinent mineral assemblages are lacking and the zircon saturation geothermometer does not apply to peralkaline systems (*e.g.*, Watson & Harrison 1983, Miller *et al*. 2003); however, some general inferences can be stated. Temperature estimates based on Ti-in-quartz geothermometry (Wark & Watson 2006) should approach liquidus temperatures, as quartz was a relatively early crystallizing phase in such high-Si peralkaline systems. Preliminary estimates made by Vilalva & Vlach (2013), assuming P = 1 kbar and an a_{TiO2} of 0.7, yield a temperature range between 650 and 800 °C for little-deformed quartz crystals from the main, undeformed, 'massive' peralkaline granite (unit C of Vilalva & Vlach 2010, *cf*. Fig. 1); in contrast, calculated temperatures drop to 400 °C in recrystallized quartz grains from the deformed facies. Of note, several samples from the main massive granites contain ferrorichterite, which is stable up to 760 °C in reduced, near WM (wüstite-magnetite) buffer conditions, and up to 535 °C under FQM (fayalite-quartz-magnetite) buffer crystallization conditions (*e.g.*, Charles 1975). Moreover, the formation of late-stage arfvedsonite in the deformed granites suggests magmatic temperatures between 800 °C (liquidus) and *ca*. 530 °C (solidus; see also Ernst 1968, Stolz 1986, Marks *et al*. 2003, Pe-Piper 2007).

As inferred above, nacareniobsite-(Ce) and britholite-(Ce) probably formed after and before submagmatic, close-to-solidus deformation, respectively, in late- magmatic crystallization environments. Considering the uncertainties of our temperature estimates and some independent inferences obtained from peralkaline systems elsewhere (*e.g.*, Marks *et al.* 2003, Macdonald 2012), it is believed that both minerals began to crystallize at temperatures ≤ 600 °C.

Mineral parageneses in peralkaline Papanduva granites point to initial melt crystallization under relatively reduced f_{O2} conditions (Vilalva & Vlach 2013). In fact, the aenigmatite-bearing, magnetite- and ilmenite-absent main, undeformed, massive peralkaline granite formed within the '*no-oxide'* field of Nicholls & Carmichael (1969), close to the FQM buffer, or below, in the case of ferrorichterite-bearing samples. These melts evolved following an oxidizing crystallization path as indicated by, among other evidence, the occurrence of late-stage aegirine mantling Na- and Na-Ca-amphiboles and the post-magmatic crystallization stage was characterized by oxidizing conditions close to the MH (magnetite-hematite) buffer (Vilalva & Vlach 2013).

Host-rock constraints on mineral compositions

The occurrence of nacareniobsite-(Ce) in oversaturated rocks, such as the peralkaline Papanduva granites and those from Madagascar (Estrade *et al*. 2011), demonstrates that its stability, and arguably that of rinkite, does not depend significantly on the Si-saturation level of the original melts. It is more probably related to the other melt compositional constrains and co-precipitating minerals in an F-rich, moderate-to-strong peralkaline crystallizing environment. As typically reported in peralkaline systems elsewhere (*e.g.*, Marks *et al.* 2003, 2011, Schilling *et al.* 2011, Vlach & Gualda 2007), both whole-rock and mineral chemical signatures indicate that melt peralkalinity increases as crystallization proceeds and is therefore relatively high in the subsequent late-magmatic stages. Furthermore, the Nb/Ti ratios in the Papanduva peralkaline granites also increase and correlate positively with the Agpaitic Index (Vilalva & Vlach 2013). Compared to nacareniobsite-(Ce) reported from occurrences of undersaturated felsic rocks, the most remarkable compositional feature of the Papanduva nacareniobsite-(Ce) is its higher Nb, Ta, (REE,Y), and, to a some extent, Na contents.

Whether the Papanduva peralkaline late-stage granites represent primary liquids or products of crystal fractionation processes, these melts were significantly enriched in Na, HFSE, and F, with low Ca abundances. Such features, along with their relatively high Nb/Ti, strongly drive reactions (1) and (2) to their left side as well as provide an opportunity for the $M^{2+} + M^{4+} = 2(REE,Y)^{3+}$ reaction, which yield (REE,Y)-rich compositions, with (REE,Y), and perhaps Na, in excess to the ideal nacareniobsite-(Ce) endmember. The same factors have influenced britholite-(Ce) compositions, which are characterized by higher contents of (REE,Y), Na, and Si compared to most of those previously reported.

Acknowledgments

We thank the Fundação de Amparo à Pesquisa do Estado de São Paulo (FAPESP, Proc. 08/00562-0) and Conselho Nacional de Desenvolvimento Científico e Tecnológico (CNPq, Proc. 305.370/2011-1) for financial support. F. Vilalva benefited from a PhD. scholarship from CNPq (Proc. 142838/2007-1) and from a Visiting Student scholarship at the University of Notre Dame from Coordenação de Aperfeiçoamento de Pessoal de Nível Superior (CAPES Foundation, Proc. BEX 4956/10-9). Comments by Dr. S. Salvi and Associate

Editor Dr. T. Birkett helped improve the original manuscript and are very much appreciated. We also thank Dr. Birkett, as well as Dr. L. Groat and Ms. M. Parker for careful editorial handling.

References

Arden, K.M. & Halden, N.M. (1999) Crystallization and alteration history of britholite in rare-earth-element-enriched pegmatitic segregations associated with the Eden Lake Complex, Manitoba, Canada. *Canadian Mineralogist* **37**, 1239–1253.

Bastin, G.F. & Heijligers, H.J.M. (1990) Progress in electron-probe micro-analysis. *Materialwissenschaft und Werkstofftechnik* **21**, 90–92.

Blenkinsop, T. (2000) *Deformation Microstructures and Mechanisms in Minerals and Rocks*. Kluwer Academic Publishers, Dordrecht, The Netherlands.

Boynton, W.V. (1984) Cosmochemistry of the rare earth elements: meteoritic studies. *In* Rare-Earth Element Geochemistry (P. Henderson, ed.). Elsevier, Amsterdam, The Netherlands, (63–114).

Cámara, F., Sokolova, E., & Hawthorne, F.C. (2011) From structure topology to chemical composition. XII. Titanium silicates: the crystal chemistry of rinkite, $Na_2Ca_4REETi(Si_2O_7)_2OF_3$. *Mineralogical Magazine* **75**, 2755–2774.

Chang, L.L.Y., Howie, R.A., & Zussman, J. (1998) *Rock-Forming Minerals. Volume 5B. Non-Silicates: Sulphates, Carbonates, Phosphates, Halides*. 2nd ed. The Geological Society, London, UK.

Charles, R.W. (1975) The phase equilibria of richterite and ferrorichterite. *American Mineralogist* **60**, 367–374.

Chen, W. & Simonetti, A. (in press) In-situ determination of major and trace elements in calcite and apatite, and U–Pb ages of apatite from the Oka carbonatite complex: Insights into a complex crystallization history. *Chemical Geology*, doi:10.1016/j.chemgeo.2012.04.022.

Ernst, W.G. (1968) *Amphiboles. Crystal Chemistry, phase relations and occurrence*. Springer-Verlag, New York, USA.

Estrade, G., Salvi, S., Béziat, D., & Soatsitohaina, R. (2011) HFSE (Zr, Nb, Hf, REE, Th, U and Ta) enrichment in peralkaline granite dykes, Ampasindava Peninsula, Madagascar. *In*: Etat des connaissances sur la géologie et la métallogénie de Madagascar au XXIème siècle. Société Géologique de France. Available online at http://sgfr.free.fr/seance/Mada2011/compte-rendu/presentation/15-Estrade_REE-Zr.pdf. (Accessed 13-03-12).

Fleet, M.E. & Pan, Y. (1995) Site preference of rare earth elements in fluorapatite. *American Mineralogist* **80**, 329–335.

Fleischer, M. (1958) Rinkite, johnstrupite, lovchorrite and calcium rinkite (all = mosandrite). *American Mineralogist* **43**, 795–796.

Fleischer, M. & Altschuler, Z.S. (1986) The lanthanides and yttrium in minerals of the apatite group – an analysis of the available data. *Neues Jahrbuch für Mineralogie (Monatshefte)* **H10**, 467–480.

Gaines, R.V., Skinner, H.C.W., Foord, E.E., Mason, B., & Rosenzweig, A. (1997) *Dana's new mineralogy*. Wiley, New York, USA.

Galli, E. & Alberti, A. (1971) The crystal structure of rinkite. *Acta Crystallographica* **B27**, 1277–1284.

Gu, J., Chao, G.Y., & Tang, S. (1994) A new mineral – fluorbritholite-(Ce). *Journal of Wuhan University of Technology* **9**, 1855–1866.

Gualda, G.A.R. & Vlach, S.R.F. (2007) The Serra da Graciosa A-type Granites and Syenites, southern Brazil. Part 1: Regional setting and geological characterization. *Anais da Academia Brasileira de Ciências* **79**, 405–430.

Harrison, T.M., Catlos, E.J., & Montel, J.-C. (2002) U-Th-Pb dating of phosphate minerals. *Reviews in Mineralogy and Geochemistry* **48**, 524–558.

Jarosewich, E. & Boatner, L.A. (1991) Rare-earth element reference samples for electron microprobe analysis. *Geostandards Newsletter* **15**, 397–399.

Kalsbeek, N., Larsen, S., & Rønsbo, J.G. (1990) Crystal structures of rare earth elements rich apatite analogues. *Zeitschrift für Kristallographie* **191**, 249–263.

Lentz, D. & Mariano, A.N. (2010) Ranking and evaluating light to heavy rare earth deposits worldwide: Exploration considerations to economic assessment. *In* 2010 PDAC International Convention, Trade Show & Investors Exchange (Toronto, Canada). Prospectors and Developers Association of Canada. Available online at http://www.slideshare.net/RareEarthsRareMetals/pdac-ree1 (Accessed 13-03-20).

Ludwig, K.R. (2003) *User´s manual for Isoplot 3.0: a geochronological toolkit for Microsoft Excel*. Berkeley Geochronological Center. *Special Publication* **4**, 71 p.

Macdonald, R. (2012) Evolution of peralkaline silicic complexes: Lessons from the extrusive rocks. *Lithos* **152**, 11–22.

Marks, M.A.W., Vennemann, T., Siebel, W., & Markl, G. (2003) Quantification of magmatic and hydrothermal processes in a peralkaline syenite–alkali granite complex based on textures, phase equilibria, and stable and radiogenic isotopes. *Journal of Petrology* **44**, 1247–1280.

Marks, M.A.W., Hettmann, K., Schilling, J., Frost, B.R., & Markl, G. (2011) The mineralogical diversity of alkaline igneous rocks: Critical factors for the transition from

miaskitic to agpaitic phase assemblages. *Journal of Petrology* **52**, 439–455.

Melluso, L., De' Gennaro, R., Fedele, L., Franciosi, L., & Morra V. (2012) Evidence of crystallization in residual, Cl-F-rich, agpaitic, trachyphonolitic magmas and primitive Mg-rich basalt-trachyphonolite interactions in the lava domes of the Phlegrean Fields (Italy). *Geological Magazine* **149**, 532–550.

Miller, C.F., Mcdowell, S.M., & Mapes, R.W. (2003) Hot and cold granites? Implications of zircon saturation temperatures and preservation of inheritance. *Geology* **31**, 529–532.

Nagy, G. (2003) Nacareniobsite-(Ce) in phonolites in the Mecsek Mts. (Hungary) – Second occurrence in the world? *The Acta Mineralogica-Petrographica Abstract Series* **1**, p.75.

Nash, W.P. (1972) Apatite chemistry and phosphorous fugacity in a differentiated igneous intrusion. *American Mineralogist* **57**, 877–886.

Nicholls, J. & Carmichael, I.S.E. (1969) Peralkaline acid liquids: a petrological study. *Contributions to Mineralogy and Petrology* **20**, 268–294.

Oberti, R., Ottolini, L., Della Ventura, G., & Parodi, G.C. (2001) On the symmetry and crystal chemistry of britholite: New structural and microanalytical data. *American Mineralogist* **86**, 1066–1075.

Orlandi, P., Perahiazzi, N., & Mannucci, G. (1989) First occurrence of britholite-(Ce) in Italy (Monte Somma, Vesuvius). *European Journal of Mineralogy* **1**, 723–725.

Pan, Y. & Fleet, M.E. (2002) Compositions of apatite-group minerals: Substitution mechanism and controlling factors. *Reviews in Mineralogy and Geochemistry* **48**, 13–49.

Parodi G.C. & Chevrier, V. (2004) New discoveries in nephelinites from Los Island (Republic of Guinea). *Bulletin de la Société Française de Minéralogie et de Cristallographie* **16**, p.5.

Pasero, M., Kampf, A.R., Ferraris, C., Pekov, I.V., Rakovan, J., & White, T.J. (2010) Nomenclature of the apatite supergroup minerals. *European Journal of Mineralogy* **22**, 163–179.

Passchier, C.W. & Trouw, R.A.J. (2005) *Microtectonics*. 2nd ed. Springer-Verlag, Berlin Heidelberg, Germany.

Pekov, I.V. & Ekimenkova, I.A. (2001) Two new rare-earth-rich mineral associations in the Ilímaussaq alkaline complex, South Greenland. *Geology of Greenland Survey Bulletin* **190**, 143–144.

Pekov, I.V., Pasero, M., Yaskovskaya, A.N., Chukanov, D., Pushcharovsky, Y., Merlino, S., Zubkova, N.V., Kononkova, N.N., Mem'shikov, P., & Zadov, A.E. (2007) Fuorcalciobritholite, $(Ca,REE)_5[(Si,P)O_4]_3F$, a new mineral: description and crystal chemistry. *European Journal of Mineralogy* **19**, 95–103.

Pe-Piper, G. (2007) Relationship of amphibole composition to host-rock geochemistry: the A-type gabbro-granite Wentworth pluton, Cobequid shear zone, eastern Canada. *European Journal of Mineralogy* **19**, 29–38.

Petersen, O.V., Rønsbo, J.G., & Leonardsen, E.S. (1989) Nacareniobsite-(Ce), a new mineral species from the Ilímaussaq alkaline complex, South Greenland, and its relation to mosandrite and the rinkite series. *Neues Jahrbuch für Mineralogie (Monatshefte)* **H2**, 84–96.

Ridolfi, F. Renzulli, A. Macdonald, R., & Upton, B.C.G. (2006) Peralkaline syenite autoliths from Kilombe volcano, Kenya Rift Valley: Evidence for subvolcanic interaction with carbonatitic fluids. *Lithos* **91**, 373–392.

Rønsbo, J.G. (1989) Coupled substitution involving REEs and Na and Si in apatites in alkaline rocks from the Ilímaussaq intrusion, South Greenland, and the petrological implications. *American Mineralogist* **74**, 896–901.

Schilling, J., Marks, M.A.W., Wenzel, T., Vennemann, T., Horváth, L., Tarassoff, P., Jacob, D.E., & Markl, G. (2011) The magmatic to hydrothermal evolution of the intrusive Mont Saint-Hilaire Complex: Insights into the late-stage evolution of peralkaline rocks. *Journal of Petrology* **52**, 2147–2185.

Slepnev, Y.S. (1957) On minerals of the rinkite group. *Izvestiia Akademii Nauk SSSR, Seriia Geologicheskaia* **3**, 63–75 (in Russian)

Sokolova, E. (2006) From structure topology to chemical composition. I. Structural hierarchy and stereochemistry in titanium dissilicate minerals. *Canadian Mineralogist* **44**, 1273–1330.

Sokolova, E. & Cámara, F. (2008) From structure topology to chemical compositions. VIII. Titanium silicates: the crystal chemistry of mosandrite from type locality of Låven (Skådön), Langesundsfjorden, Larvik, Vestfold, Norway. *Mineralogical Magazine* **72**, 887–897.

Sokolova, E. & Hawthorne, F.C. (2008) From structure topology to chemical composition. V. Titanium silicates: The crystal chemistry of nacareniobsite-(Ce). *Canadian Mineralogist* **46**, 1333–1342.

Stolz, A.J. (1986) Mineralogy of the Nandewar Volcano, Northeastern New South Wales, Australia. *Mineralogical Magazine* **50**, 241–255.

Strunz, H. & Nickel, E.H. (2001) *Strunz mineralogical tables: Chemical-structural mineral classification system*. Schweizerbart'sche, Stuttgart, Germany.

Van Achterbergh, E., Ryan, C., Jackson, S., & Griffin, W. (2001) Appendix 3: Data reduction software for LA-ICP-MS. *In* Laser-Ablation-ICPMS in the Earth Sciences. *Mineralogical Association of Canada Short Course* **29**, 239–243.

VILALVA, F.C.J. (2007) *Petrografia e mineralogia de granitos peralcalinos: O Plúton Papanduva, Complexo Morro Redondo (PR/SC)*. Unpublished MSc thesis, Instituto de Geociências, Universidade de São Paulo, São Paulo, Brazil. Available online at http://www.teses.usp.br/teses/disponiveis/44/44143/tde-14122007-093212/en.php.

VILALVA, F.C.J. & VLACH, S.R.F. (2010) Major- and trace-element composition of REE-rich turkestanite from peralkaline granites of the Morro Redondo Complex, Graciosa Province, south Brazil. *Mineralogical Magazine* **74**, 645–658.

VILALVA, F.C.J. & VLACH, S.R.F. (2013) Geology, petrography and geochemistry of the A-type granites from the Morro Redondo Complex (PR-SC), South Brazil, Graciosa Province. *Anais da Academia Brasileira de Ciências*, (in press).

VLACH, S.R.F. (2010) Th-U-Pb_T dating by electron probe microanalysis, Part I. Monazite: analytical procedures and data treatment. *Geologia USP. Série Científica* **10**, 61–85.

VLACH, S.R.F. (2012) Micro-structural and compositional variations of hydrothermal epidote-group minerals from a peralkaline granite, Corupá Pluton, Graciosa Province, South Brazil, and their petrological implications. *Anais da Academia Brasileira de Ciências* **84**, 407–425.

VLACH S.R.F. & GUALDA, G.A.R. (2007) Allanite and chevkinite in A-type granites and syenites of the Graciosa Province, southern Brazil. *Lithos* **97**, 98–121.

VLACH, S.R.F. & VILALVA, F.C.J. (2007) Ocorrência de narsarsukita, britholita-(Ce) e nacareniobsita-(Ce) em granitos peralcalinos do Complexo Morro Redondo (PR/SC), Província Graciosa. *In* XI Congresso Brasileiro de Geoquímica (Atibaia – SP). SBGq.

VLACH, S.R.F., SIGA JR, O., HARARA, O.M., GUALDA, G.A.R., BASEI, M.A.S., & VILALVA, F.C.J. (2011) Crystallization ages of the A-type magmatism of the Graciosa Province (Southern Brazil): Constraints from zircon U-Pb (ID-TIMS) dating of coeval K-rich gabbro-dioritic rocks. *Journal of South American Earth Sciences* **32**, 407–415.

WARK, D.A. & WATSON, E.B. (2006) TitaniQ: a titanium-in-quartz geothermometer. *Contributions to Mineralogy and Petrology* **152**, 743–754.

WATSON, E.B. & HARRISON, T.M. (1983) Zircon saturation revisited: temperature and composition effects in a variety of magma types. *Earth and Planetary Science Letters* **64**, 295–304.

WINTHER, C. (1901) Britolith, ein in neues mineral. *Zeitschrift für Kristallographie und Mineralogie* **34**, 685–687.

Received July 26, 2012, revised manuscript accepted March 25, 2013.